

Uncertainty of low-degree space gravimetry observations: surface processes versus internal signal

Hugo Lecomte¹, Severine Rosat², Mioara Manda³, Jean-Paul Boy⁴, and Julia Pfeffer⁵

¹ITES (CNRS UMR7063), Université de Strasbourg

²IPGS-EOST

³Centre National d'Etudes Spatiale

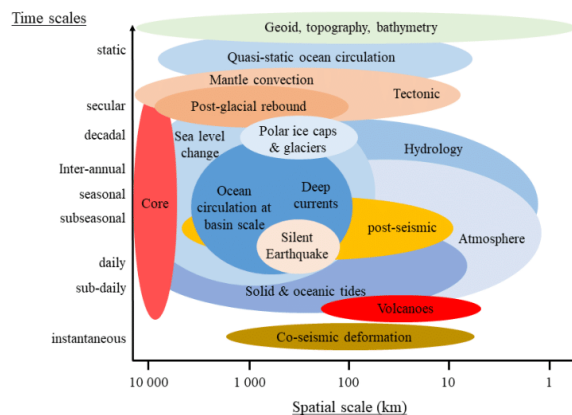
⁴IPGS-EOST, CNRS/University of Strasbourg

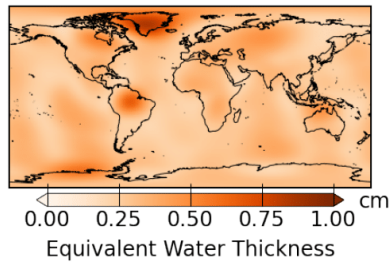
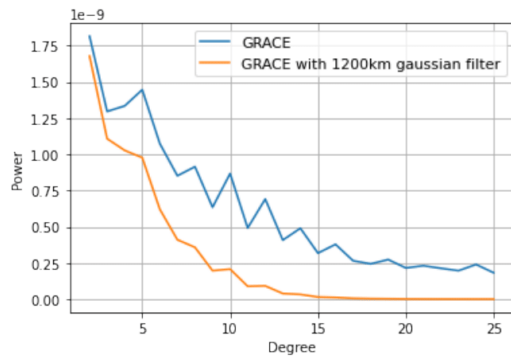
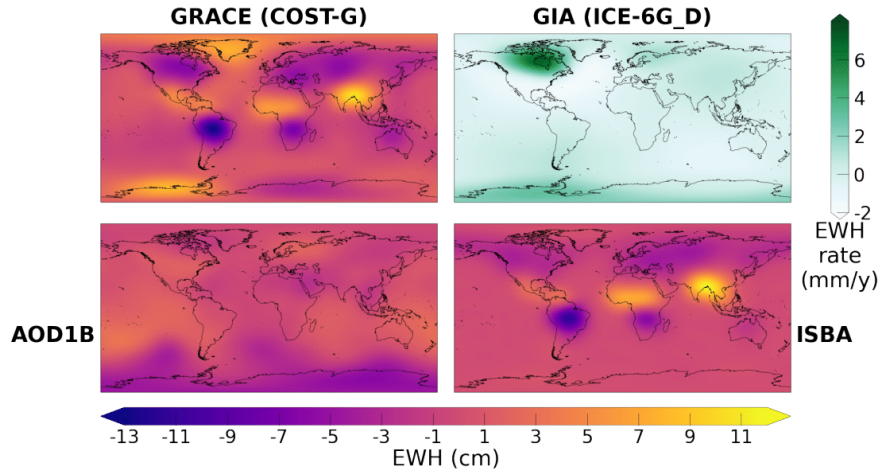
⁵Magellium

March 1, 2023

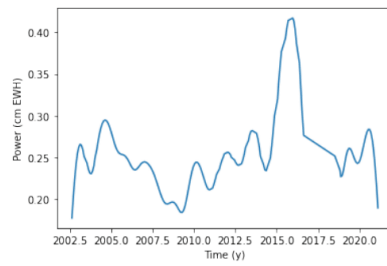
Abstract

Space gravity measurements have been mainly used to study the temporal mass variations at the Earth's surface and within the mantle. Nevertheless, mass variations due to the Earth's core might be observable in the gravity field variations as measured by GRACE(-FO) satellites. Earth's core dynamical processes inferred from geomagnetic field measurements are characterized by large-scale patterns associated with low spherical harmonic degrees of the potential fields. To study these processes, the use of large spatial and inter-annual temporal filters is needed. To access gravity variations related to the Earth's core, surface effects must be corrected, including hydrological, oceanic or atmospheric loading (Newtonian attraction and mass redistribution). However, these corrections for surface processes add errors to the estimates of the residual gravity field variations enclosing deep Earth's signals. As our goal is to evaluate the possibility to detect signals of core origin embedded in the residual gravity field variations, a quantification of the uncertainty associated with gravity field products and geophysical models used to minimise the surface process signatures is necessary. Here, we estimate the dispersion for GRACE solutions as about 0.34 cm of Equivalent Water Height (EWH) or 20% of the total signal. Uncertainty for hydrological models is as large as 0.89 to 2.10 cm of EWH. We provide estimates of Earth's core signals whose amplitudes are compared with GRACE gravity field residuals and uncertainties. The results presented here underline how challenging is to get new information about the dynamics of the Earth's core via high-resolution, high-accuracy gravity data.

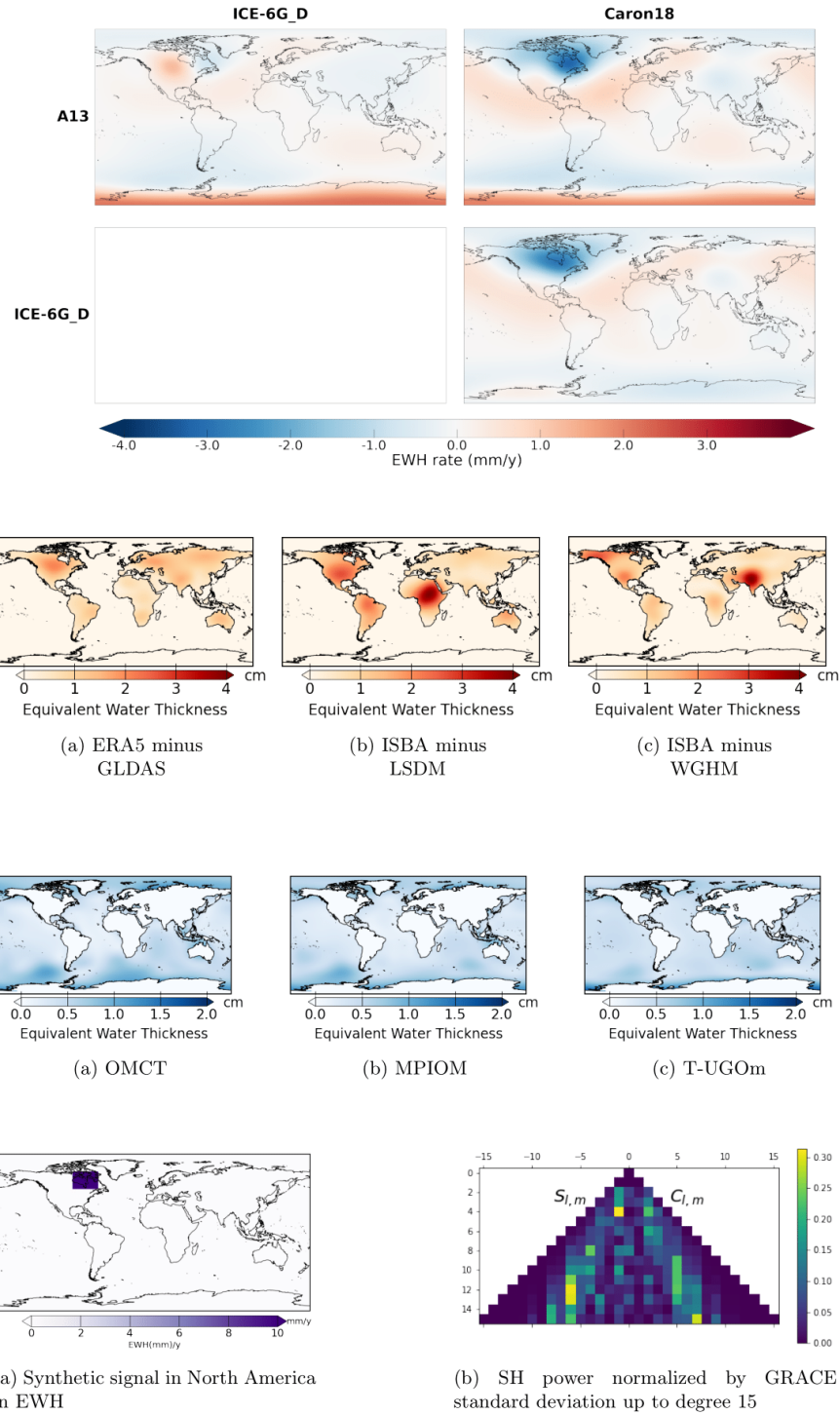


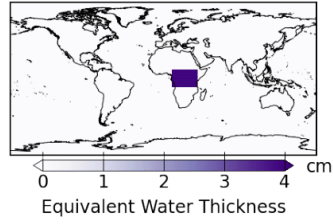


(a) Average of RMS differences in cm EWH spatially represented

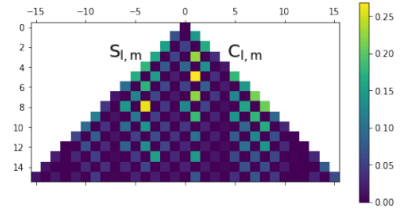


(b) Average of RMS differences in cm EWH represented through time

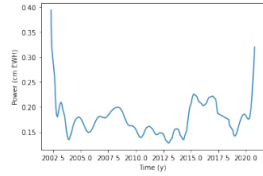




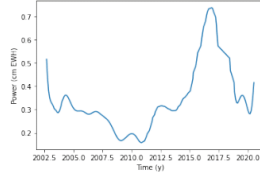
(a) Synthetic 3-yr signal over Africa with an amplitude of 4 cm EWH



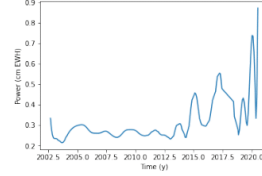
(b) SH power normalized by GRACE standard deviation up to degree 15



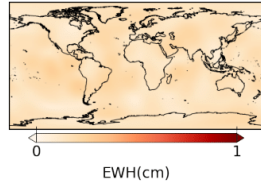
(a) Temporal RMS difference between CSR and JPL solutions



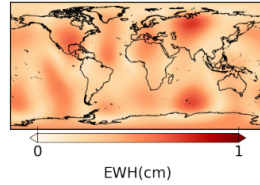
(b) Temporal RMS difference between CSR and GFZ solutions



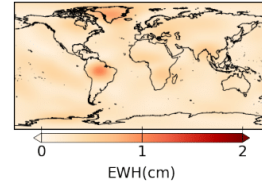
(c) Temporal RMS difference between CSR and GRAZ solutions



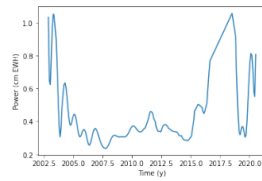
(d) Spatial RMS difference between CSR and JPL solutions



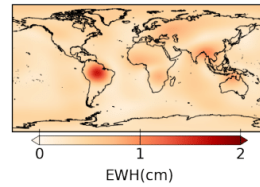
(e) Spatial RMS difference between CSR and GFZ solutions



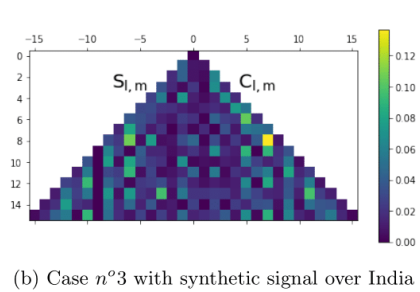
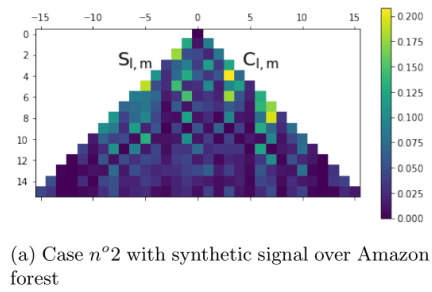
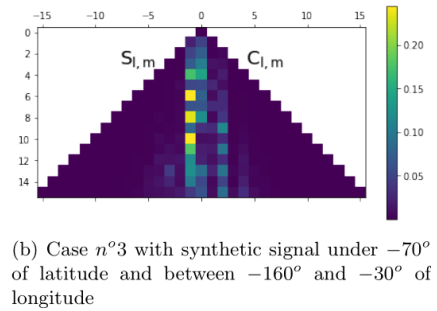
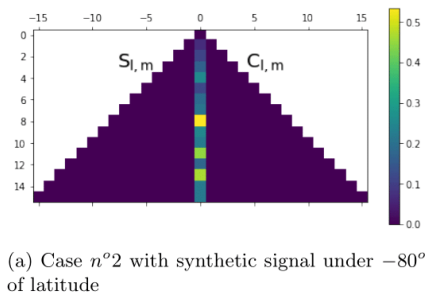
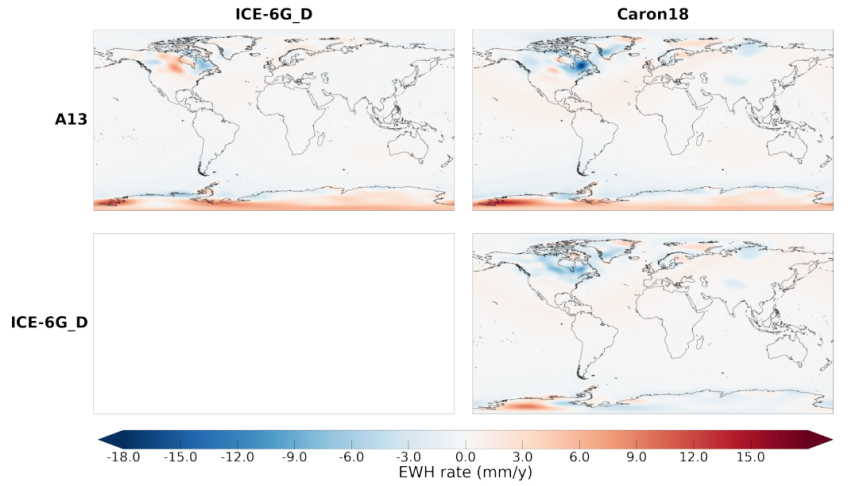
(f) Spatial RMS difference between CSR and GRAZ solutions



(g) Temporal RMS difference between CSR and CNES solutions



(h) Spatial RMS difference between CSR and CNES solutions



1 **Uncertainty of low-degree space gravimetry**
2 **observations: surface processes versus internal signal**

3 **Hugo Lecomte¹, Séverine Rosat¹, Mioara Manda², Jean-Paul Boy¹, Julia**
4 **Pfeffer³**

5 ¹Université de Strasbourg, CNRS, EOST, ITES UMR7063, F-67000 Strasbourg, France

6 ²Centre National d'Etudes Spatiales, Paris, France

7 ³Magellium, Ramonville Saint-Agne, France

8 **Key Points:**

- 9 • Deep Earth's processes occur at large spatial and inter-annual temporal scales
- 10 • Time-lapse gravity satellite data are compared with geophysical models at scales
11 of interest
- 12 • Large uncertainties on satellite data and geophysical models conceal the gravity
13 signals originated from the Earth's core

Corresponding author: Hugo Lecomte, hlecomte@unistra.fr

Abstract

Space gravity measurements have been mainly used to study the temporal mass variations at the Earth's surface and within the mantle. Nevertheless, mass variations due to the Earth's core might be observable in the variations of the gravity field as measured by GRACE(-FO) satellites. Earth's core dynamical processes inferred from geomagnetic field measurements are characterized by large-scale patterns associated with low spherical harmonic degrees of the potential fields. To study these processes, the use of large spatial and inter-annual temporal filters is needed. To access gravity variations related to the Earth's core, surface effects must be corrected, including hydrological, oceanic or atmospheric loading (Newtonian attraction and mass redistribution associated with elastic deformation). However, these corrections for surface processes add errors to the estimates of the residual gravity field variations enclosing deep Earth's signals. As our goal is to evaluate the possibility to detect signals of core origin embedded in the residual gravity field variations, a quantification of the uncertainty associated with gravity field products and geophysical models used to minimise the surface process signatures is necessary. Here, we estimate the dispersion for GRACE solutions as about 0.34 cm of Equivalent Water Height (EWH) or 20% of the total signal. Uncertainty for hydrological models is as large as 0.89 to 2.10 cm of EWH. We provide estimates of some Earth's core signals which amplitudes are compared with GRACE gravity field residuals and uncertainties. The results presented here underline how challenging is to get new information about the dynamics of the Earth's core via high-resolution, high-accuracy gravity data.

Plain Language Summary

The motions of the Earth's fluid core are deduced from ground and satellite measurements of the geomagnetic field variations. Because the long-term variations of the Earth's gravity field might be correlated to the Earth's magnetic field, new information about the Earth's fluid core and its density changes could be accessed with gravimetry. The observation of the core processes must be done at very large spatial scales, in which case it is necessary to use gravity data from satellites. However, variations in the Earth's gravity field are also created by heterogeneous superficial sources such as ocean and atmospheric currents, variations in water storage, etc. To recover a signature of the Earth's fluid core, we need first to remove all other known effects of larger amplitudes from satellite observations of the gravity field. Our study compares models of gravity variations for different sources

46 in order to estimate their uncertainty. Such uncertainties are discussed in view of the
47 expected amplitudes of signals originated from the core.

1 Introduction

Gravity field variations measured by the Gravity Recovery and Climate Experiment (GRACE) and GRACE Follow-On (GRACE-FO) missions are sensitive to the redistribution of masses located above, at or below the Earth's surface (Chen et al., 2022). GRACE & GRACE-FO (referred to as GRACE) satellite data are used to estimate the Earth's mass variations from regional to global scales since 2002 (Tapley et al., 2004; Landerer et al., 2020). For example, GRACE satellite data became essential to monitor the evolution of terrestrial water storage, ice sheets, glaciers and sea level in a worldwide changing climate (Tapley et al., 2019). GRACE satellite data are, by nature, integrative, so that it may be difficult to separate the sources of change in the gravity field. Each process has a specific spatial and temporal signature that can go from global to local and from the secular to the sub-daily scales (Fig. 1). We refer to certain surface processes with the term "loading" defined here as the Newtonian attraction and mass redistribution associated with elastic deformation. By approximate order of magnitude, the processes include in GRACE records are tidal effects from extraterrestrial bodies, post-glacial rebound (Purcell et al., 2011), hydrological (Rodell et al., 2018), atmospheric (Kusche & Schrama, 2005) and oceanic (Dobslaw et al., 2017) loading, water mass displacement across ocean, hydrosphere and cryosphere (Pfeffer et al., 2021), pre-seismic (Bouih et al., 2022), co-seismic and post seismic (Deggim et al., 2021) mass re-distributions, sea level changes (Adhikari et al., 2019; Horwath et al., 2022) and finally core processes.

In addition to its primary purposes, some new applications of the GRACE measurements were proposed to study the deep Earth's interior. Panet et al. (2018) gave an example of possible seismic precursor in the mantle before Tohoku earthquake in 2011; this kind of signature was also observed before the Maule-Chile event (Bouih et al., 2022). Other authors have proposed to improve the knowledge of the dynamical processes of the Earth's core. Dumberry (2010a); Dumberry and Manda (2021) predicted a gravity perturbation generated by various core processes that might be observable on the low degrees of the gravity field. No signature of these perturbations has yet been observed in the gravity variations. However, Manda et al. (2012) showed a correlation between the variations of the geomagnetic field and the gravity field. Processes of dissolution and crystallization at the core-mantle boundary (CMB) were advocated to explain this correlation (Manda et al., 2015).

80 Established methods of seismic tomography, Earth’s rotation, gravity and geomagnetic
 81 data analysis and geodynamic modelling constrain distributions of seismic velocity, density,
 82 electrical conductivity, and viscosity at depth, all depending on the internal structure
 83 of the Earth. Global Earth’s interior models based on different observables often lead
 84 to rather different images. For example, the analysis of the time-variable magnetic field
 85 allows to focus on the dynamical features of the core field (Gillet et al., 2010, 2022). On
 86 the other hand, gaining information about the Earth’s core from the analysis of the gravity
 87 field is difficult, because it requires to separate the different sources of signal with independent
 88 observations and/or models. In this context, gravimetry has the potential to bring new
 89 constraint about the density anomalies in the core and at its boundaries in a complimentary
 90 way to seismology (Koelemeijer, 2021).

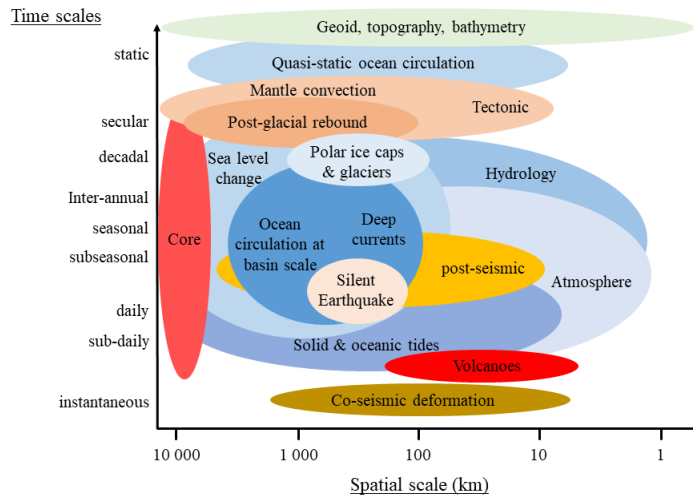


Figure 1: Spatial and temporal scales of the physical processes causing mass variations in the Earth system *adapted from Ilk et al. (2004)*

91 One way to extract the Earth’s core signal from gravity observations is to use independent
 92 information from models of shallower sources (i.e. water mass redistribution in the hydrosphere,
 93 ocean, atmosphere, cryosphere and solid Earth’s processes associated with earthquakes
 94 and glacial isostatic adjustment) to remove such larger amplitude contributions and to
 95 study the remaining signal. In this paper, we propose different models of post-glacial rebound,
 96 hydrological, atmospheric and oceanic mass redistribution for this purpose. The main

97 objective of this work is to estimate the uncertainty associated with each category of models
 98 at large spatial scales over 1200 km and inter-annual time scales to compare with the
 99 expected gravitational signature of some core processes. This estimation can not be done
 100 for the earthquakes and for the cryosphere because the existing models are not independent
 101 from GRACE observations (Deggim et al., 2021; Adhikari et al., 2016).

102 To our knowledge, there was no published study evaluating gravity field products
 103 and models at these scales. A first paper in this direction has assessed the accuracy of
 104 satellite laser ranging (SLR) and hydrological loading products at inter-annual time-scales
 105 and for degree-2 as compared with surface deformation from GNSS (Rosat et al., 2021).
 106 They showed that the gravity and surface deformation signatures of inter-annual degree-
 107 2 pressure flows at the CMB are much lower than the observed uncertainties.

108 Here we focus on the gravitational signature induced by various core processes that
 109 are firstly presented (2). We then present the spherical harmonics (SH) products and
 110 geophysical models used to estimate gravity variations (3). A minimum threshold of uncertainty
 111 is provided for each category of products and models (4). These uncertainties are finally
 112 discussed and compared with expected amplitudes of the presented core processes (5).

113 2 Expected gravitational signals from the Earth’s core

114 Dynamical core processes disturb the time-varying gravity field through the direct
 115 Newtonian effect of mass anomalies in the fluid core. Dynamical core processes also have
 116 indirect effects, such as pressure changes at the CMB induced by varying core flows or
 117 changes in the rotation vector of the solid Earth. Dumberry and Manda (2021) provided
 118 a review of the surface deformation and gravity variations induced by core dynamics, as
 119 well as a quantification of the expected amplitudes. In this part, we aim to provide a brief
 120 summary of these effects and an estimation of the amplitude in Equivalent Water Height
 121 (EWH) at the temporal scales observable with GRACE.

122 2.1 Spherical Harmonics (SH) representation

123 In the following, we note $C_{l,m}$ and $S_{l,m}$ the degree- l , order- m fully normalized Stokes
 124 coefficients of the SH representation of the Earth’s gravitational potential. With $\hat{C}_{l,m}$
 125 and $\hat{S}_{l,m}$ the unnormalized coefficients and $\delta_{m,0}$ the Kronecker delta, the normalization
 126 is given by:

$$\begin{bmatrix} C_{l,m} \\ S_{l,m} \end{bmatrix} = \sqrt{\frac{(n+m)!}{(2-\delta_{m,0})(2n+1)(n-m)!}} \begin{bmatrix} \hat{C}_{l,m} \\ \hat{S}_{l,m} \end{bmatrix} \quad (1)$$

The amplitude of the Stokes coefficient can be represented as EWH. An EWH amplitude, $\Delta\sigma(\lambda, \phi)$ is function of the longitude λ and the latitude ϕ (Wahr et al., 1998):

$$\Delta\sigma(\lambda, \phi) = \frac{R\bar{\rho}}{3\rho_w} \sum_{l=0}^{\infty} \sum_{m=0}^l \frac{2l+1}{1+k_l} [\Delta C_{l,m} \cos(m\lambda) + \Delta S_{l,m} \sin(m\lambda)] \bar{P}_l^m(\cos\phi), \quad (2)$$

127 where $\bar{P}_l^m(\cos\phi)$ are the associated fully normalized Legendre polynomials (4π normalization).
 128 R is the Earth's radius (6.371×10^6 m), $\bar{\rho}$ is the mean density of the Earth (5515 kg.m^{-3}),
 129 ρ_w is the density of water (1000 kg.m^{-3}) and k_l is the load Love number of degree l .

130 2.2 Newtonian effect of mass anomalies in the fluid core

131 Core flows create redistribution of density anomalies (Dumberry, 2010a). This first
 132 perturbation leads to an adjustment in the internal stress field. A secondary density perturbation
 133 is then created because of a global elastic deformation, due to this stress field.

A density perturbation, $\Delta\rho(r, \lambda, \phi)$ is function of the radius r , the longitude λ and the latitude ϕ . There is an expansion in SH for each radius r :

$$\Delta\rho(r, \lambda, \phi) = \sum_{l=0}^{\infty} \sum_{m=0}^l [\rho_{l,m}^c(r) \cos(m\lambda) + \rho_{l,m}^s(r) \sin(m\lambda)] \bar{P}_l^m(\cos\phi) \quad (3)$$

The gravity variation created by this density perturbation can be expressed as a SH coefficient variation of the gravity field, $\Delta C_{l,m}$ or $\Delta S_{l,m}$, by integrating the density perturbation for each radius in the fluid core between the Inner Core Boundary (ICB) and the CMB (Dumberry, 2010a).

$$\Delta C/S_{l,m} = \frac{4\pi}{2l+1} \frac{1}{MR^l} \int_{r_{ICB}}^{r_{CMB}} \rho_{l,m}^{c/s}(r) [1 + \kappa_l(r)] r^{l+2} dr, \quad (4)$$

134 where M corresponds to the mass of the Earth (5.972×10^{24} kg) and $\kappa_l(r)$ characterize
 135 the additional contribution due to global elastic deformation at degree l and radius r .
 136 $\kappa_l(r)$ values comes from Dumberry (2010a) and for degree $l > 2$, they fall within the
 137 range of approximately 0.2 and -0.2.

138 To have an order of amplitude of the gravitational effect created by density anomalies,
 139 we can take upper bound values for the density variations. The amplitude of density variations

140 within the Earth’s core increases with the time scale of the analysis. This is because longer
 141 time scales allow for the observation of larger and more gradual changes in the density
 142 of the core, such as those caused by large-scale convection patterns (Dehant et al., 2022).
 143 At decadal and inter-annual time scales (maximal time-length achievable, yet, with GRACE
 144 observations), the upper bound of the density variation is $\Delta\rho = 1 \times 10^{-5} \text{ kg.m}^{-3}$ (Dumberry
 145 & Manda, 2021). For an annual period, this amplitude is smaller by one order of magnitude.

146 Supposing as an upper bound a variation with an amplitude of $\Delta\rho = 1 \times 10^{-5} \text{ kg.m}^{-3}$
 147 at each radius of the fluid core, we compute the effect for degree $l = 2, 6$ and 10 . At inter-
 148 annual and decadal time scales, this gives respective Stokes coefficient variations of $2 \times$
 149 10^{-11} , 1×10^{-13} and 4×10^{-15} . This values can be estimated in cm EWH and for degree
 150 $2, 6$ and 10 , we respectively obtain as upper-bound values $0.1, 0.006$ and 0.0005 cm EWH,
 151 over a decadal period.

152 **2.3 Pressure flows effect**

153 Besides the direct Newtonian effect, core flows create a tension on the CMB. This
 154 tension results in elastic deformations of the boundary and therefore, density perturbation
 155 (Dumberry, 2010a; Dumberry & Bloxham, 2004a). The same process occurs at the ICB.

In the same way as for density perturbation, we can describe the pressure anomalies
 $\Delta p(\lambda, \phi)$ with an expansion in SH at the CMB :

$$\Delta p(\lambda, \phi) = \sum_{l=0}^{\infty} \sum_{m=0}^l [p_{l,m}^c(r) \cos(m\lambda) + p_{l,m}^s(r) \sin(m\lambda)] \bar{P}_l^m(\cos \phi) \quad (5)$$

The gravity variations created by these pressure anomalies can be expressed as a
 SH coefficient variation of the gravity field $\Delta C_{l,m}$ or $\Delta S_{l,m}$ (Dumberry, 2010a) :

$$\Delta C/S_{l,m} = \bar{k}_l \frac{R}{GM\bar{\rho}} p_{l,m}^{c/s}(r), \quad (6)$$

156 where G is the gravitational constant ($6.674 \times 10^{-11} \text{ m}^3 \text{ kg}^{-1} \text{ s}^{-2}$) and \bar{k}_l are potential
 157 Love numbers corresponding to degree l . For degree $2, 6$ and 10 , \bar{k}_l values are respectively
 158 1.116×10^{-1} , 1.957×10^{-3} and 9.856×10^{-5} (Dumberry & Manda, 2021).

159 To have an order of amplitude of the gravitational effect created by pressure anomalies,
 160 we can use typical pressure variations. As for the density, the pressure amplitude is dependent
 161 on the period. As the time scale of the analysis increases, the amplitude of the pressure
 162 variations also increases (Gillet et al., 2020). At decadal and inter-annual time scales,

163 the typical pressure variations at the CMB should be $\Delta p = 100$ Pa (Dumberry & Manda, 2021). For annual period, this amplitude is one order of magnitude smaller.
164

165 Supposing as an upper bound a variation with an amplitude of $\Delta p = 100$ Pa at
166 the CMB, we compute the effect for degree $l = 2, 6$ and 10 . At inter-annual and decadal
167 time scales, this gives Stokes coefficient variations of 3×10^{-11} , 6×10^{-13} and 3×10^{-14}
168 and corresponding EWH of 0.5 , 0.04 and 0.004 cm EWH, over a decadal period.

169 **2.4 Specific effects on degree 2 of the gravity field**

170 We have previously discussed two mechanisms responsible for generating mass variations
171 at different length scales. However, there are processes like alteration of the rotation vector
172 and inner core reorientation that also lead to degree 2 variations :

173 **2.4.1 Rotation effects of the core**

174 Core dynamics can cause variations in the gravitational field through the alteration
175 of the rotation vector of the solid Earth. For example, the exchange of angular momentum
176 between the core and mantle produces changes in the angular velocity of the Earth, also
177 express as Length of Day (LOD) variations. Pressure flows are responsible for decadal
178 LOD variations (Jault & Finlay, 2015). Because Earth's angular momentum must be
179 conserved, a change in the Earth's oblateness ($J_2 = -\sqrt{5}C_{2,0}$) is associated with a change
180 in rotation. A 50 Pa change in $p_{2,0}$ at decadal periods result in $J_2 \approx 8 \times 10^{-12}$ (Gillet
181 et al., 2020). This corresponds to $C_{2,0} \approx 4 \times 10^{-12}$ and 0.06 cm EWH.

182 A similar computation for the inner core rotation creates a variation of $C_{2,0}$ term
183 that is five orders of magnitude lower (Dumberry & Bloxham, 2004b). It can then be
184 ignored.

185 **2.4.2 Inner Core reorientation**

186 The inner core is supposed to have a topography at degree 2 and order 2, $h_{2,2}$. When
187 the inner core is tilted by an angle α , it creates a variation on the coefficient $S_{2,2}$. This
188 variation can be approximated by :

$$\Delta S_{2,2} \approx 10^{-10} h_{2,2} \alpha \quad (7)$$

189 under the hypothesis of a non-convecting inner core and with a density almost uniform
 190 at hydrostatic equilibrium (Dumberry, 2010b).

191 Dumberry and Manda (2021) estimated the amplitude of the inner core reorientation
 192 supposing $\alpha = 0.4^\circ$ and $h_{2,2} = 18$ m on decadal time period. It gives $\Delta S_{2,2} = 10^{-11}$
 193 and 0.2 cm EWH.

194 **2.5 Summary of the gravitational signals from the Earth’s core**

195 The table 1 presents the amplitude of mass variations due to various core processes
 196 at different degree in EWH. The amplitude observed by GRACE is at least one order
 197 of magnitude larger than the predicted effects. Density anomalies have the lowest amplitude
 198 at degree 2 (0.1 cm EWH) and strongly decrease as the degree increases. These results
 199 suggest that mass variations due to core processes are most prominent at small degrees,
 200 and strongly decrease at higher degrees.

201 This observation is consistent with Rosat et al. (2021), which reports that at spherical
 202 harmonic degree 2, the contribution of core processes to gravity variations and ground
 203 deformations is approximately 10 times smaller than the observed fluctuations caused
 204 by dynamical processes within the fluid layers at the Earth’ surface.

Table 1: Decadal amplitude of mass variations due to core processes at different degree in cm EWH

| Gravitational effect | EWH (cm) | | |
|-----------------------------|----------|----------|-----------|
| | Degree 2 | Degree 6 | Degree 10 |
| Amplitude observed by GRACE | 5 | 20 | 15 |
| Density anomalies | 0.1 | 0.006 | 0.0005 |
| CMB Pressure anomalies | 0.5 | 0.04 | 0.004 |
| Inner core rotation | 0.2 | X | X |

205 This section points out that the study of the Earth’s core through gravity field variations
 206 can, yet, only be done at large spatial scales and inter-annual / decadal time scales. Consequently,

207 identifying signals of core origin poses a significant challenge and requires accurate removal
 208 of all surface effects.

209 3 Data presentation

210 Solutions for the time-variable gravity field are obtained using GRACE measurements
 211 with SLR measurements for low degrees. Geophysical models representing hydrological,
 212 oceanic and glacial isostatic adjustment (GIA) processes are obtained from independent
 213 models and not from GRACE inputs.

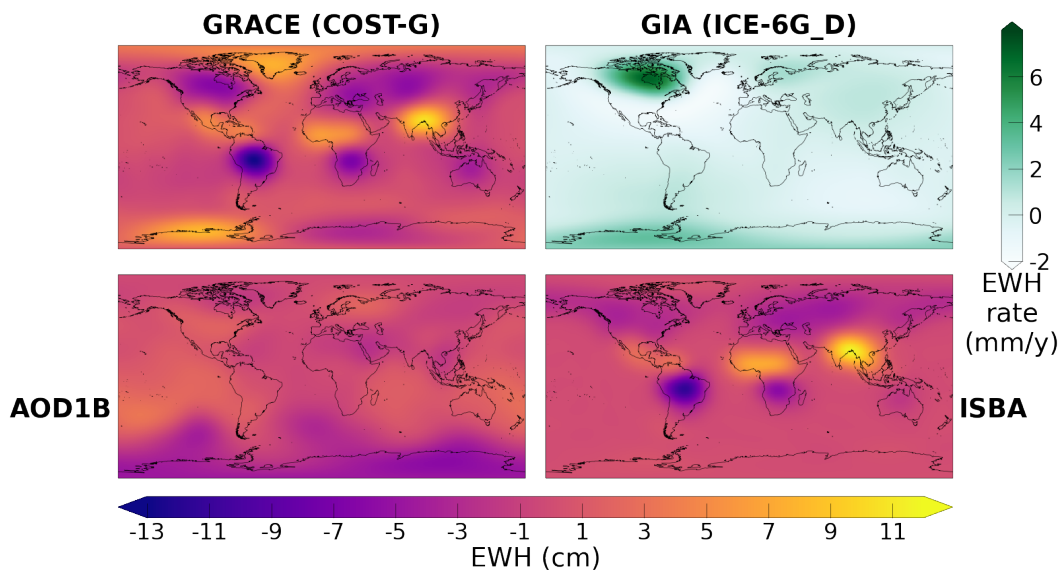


Figure 2: Surface mass in September 2008 estimated with the GRACE solution from the COST-G center (top left panel), the atmospheric and oceanic circulation model AOD1B (bottom left panel), the hydrological model Interaction Sol-Biosphère-Atmosphère (ISBA) (bottom right model) and GIA rate height change from ICE-6G_D (VM5a) model; a spatial filtering as detailed in 3.1

214 3.1 Mathematical approach

215 Models and solutions are provided in either spherical harmonics (SH) or grid representation
 216 (Swenson & Wahr, 2002). Since we are interested in large spatial scales, we primarily
 217 use SH processing and representation. We only use the grid format to represent our results

218 in a geographically interpretable way. Spatial representations are presented in Equivalent
 219 Water Height (EWH) (Fig. 2).

220 To study hypothetical gravity variations originating from the Earth’s core, we filter
 221 the products and models considered in this study at appropriate spatial and temporal
 222 scales (Section: 2.5). The spatial filtering is done with a Gaussian filter (Jekeli, 1981)
 223 of radius 1200 km to access large spatial scales and avoid Gibbs aliasing. We do not use
 224 the usual isotropic spatial filter (Kusche, 2007) that allows to recover high resolution signals.
 225 Post-filtered SH are increasingly reduced to degree 12 because of the Gaussian filter (Fig.
 226 3). The temporal filtering is done with a Butterworth low-pass filter with a cut-off period
 227 at 2 years. This removes high-amplitude signals with annual and semi-annual periods
 228 in the products and models.

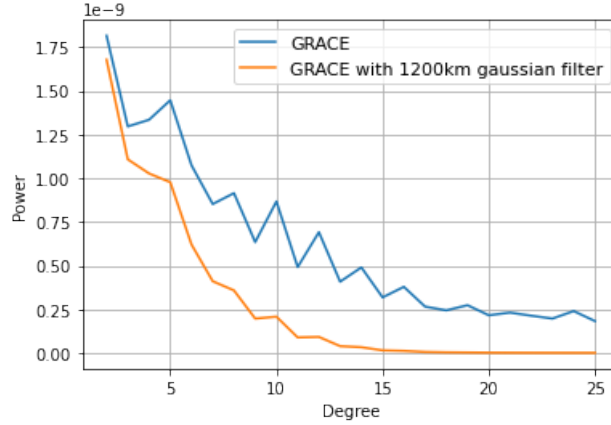


Figure 3: Power of SH degree for GRACE with and without spatial filtering up to degree
 25

229 3.2 GRACE

230 GRACE gravity-field SH solutions are distributed by several analysis centers, providing
 231 GRACE Satellite-only Model (GSM) coefficients of the geopotential (Bettadpur, 2018).
 232 In this study, we considered 6 GSM solutions (see 2 for details) from the 3 Science Data
 233 System centers (Center for Space Research (CSR) (*CSR RL6.0*, 2018), German Research
 234 Centre for Geosciences (GFZ) (Dahle et al., 2019) and Jet Propulsion Laboratory (JPL)
 235 (*JPL RL6.0*, 2018)) and 3 non-official centers (International Combination Service for
 236 Time-variable Gravity Fields (COST-G) (Meyer et al., 2020), Institute of Geodesy at

237 Graz University of Technology (IFG-TU GRAZ) (Mayer-Gürr et al., 2018) and Centre
 238 national d’études spatiales (CNES) (Lemoine et al., 2019)). GRAZ and CNES centers
 239 propose different approaches: sub-monthly hydrological de-aliasing for GRAZ, addition
 240 of SLR inputs for low degree determination for CNES. COST-G is a combination of the
 241 solutions from the other 5 centers used in this paper with the addition of Astronomical
 242 Institute University Bern (AIUB) solution. Detailed information about considered solutions
 243 are given in Table 2.

244 The 6 GRACE solutions considered in this study have a quasi-monthly time resolution.
 245 Time series span from the start of the GRACE mission, April 2002, to April 2021. There
 246 is a gap of one year between mid-2017 and mid-2018 between the GRACE and the GRACE-
 247 FO missions. As we are interested in the low degrees of the gravity field variations, we
 248 use only spherical harmonics (SH) models and not MASCON products. SH solutions are
 249 global whereas MASCON products are designed to access higher spatial resolution with
 250 pre-established grid that are an a priori of the mass distribution (Scanlon et al., 2016).
 251 Others institutes propose GRACE solutions, but they are not considered here.

Table 2: Characteristics of the GRACE gravity-field models

| Model | Mean Gravity Field Model | Ocean Tides | Atmospheric mass variations | Oceanic non-tidal mass variations | Data sources | Reference |
|----------------|----------------------------|----------------------------|---|-----------------------------------|---|---------------------------|
| CSR RL06 | GGM05C | GOT4.8 | AOD1B RL06 GAA | AOD1B RL06 GAB | https://podaac-tools.jpl.nasa.gov/drive/ | (CSR RL6.0, 2018) |
| GFZ RL06 | GGM05C | FES2014b | AOD1B RL06 GAA | AOD1B RL06 GAB | https://podaac-tools.jpl.nasa.gov/drive/ | (Dahle et al., 2019) |
| JPL RL06 | EIGEN-6C4 | FES2014 | AOD1B RL06 GAA | AOD1B RL06 GAB | https://podaac-tools.jpl.nasa.gov/drive/ | (JPL RL6.0, 2018) |
| ITSG-Grace2018 | ITSG-GraceGoce2017 | FES2014b + GRACE estimates | AOD1B RL06 GAA and LSDM for sub-monthly hydrology de-aliasing | AOD1B RL06 GAB | https://icgem.gfz-potsdam.de/ | (Mayer-Gürr et al., 2018) |
| CNES RL05 | EIGEN-GRGS.RL04.MEAN-FIELD | FES2014b | 3-D ECMWF ERA-Interim + AOD1B RL06 GAA | TUGO + AOD1B RL06 GAB | https://grace.obs-mip.fr/ | (Lemoine et al., 2019) |
| COST-G RL01 | X | X | X | X | https://icgem.gfz-potsdam.de/ | (Meyer et al., 2020) |

252 The $C_{2,0}$ estimation with GRACE data is affected by a disturbing 161-day periodic
 253 signal (Chen et al., 2005; Cheng & Ries, 2017) without a consensual explanation for this

254 issue. It has then become a standard to replace the GRACE determination of $C_{2,0}$ by
 255 the SLR one. We use the Technical notes TN14 solution based on SLR data and recommended
 256 in Loomis et al. (2019a). The GRACE $C_{3,0}$ is also poorly observed when the satellites
 257 pair is operating without two fully functional accelerometers (Loomis et al., 2020). The
 258 TN14 solution also provides a $C_{3,0}$ estimation that we include after October 2016 (GRACE
 259 month > 178). These two problematic estimations are suspected to also affect other coefficients
 260 such as $C_{4,0}$, $C_{5,0}$ and $C_{6,0}$ (Cheng & Ries, 2017; Sośnica et al., 2015; Loomis et al., 2020).
 261 However, the quality of these GRACE coefficients is comparable with the quality of the
 262 SLR coefficient estimation (Cheng & Ries, 2017; Velicogna et al., 2020). It seems then
 263 not relevant to replace these coefficients. Dahle et al. (2019) suggested to have a special
 264 attention to $C_{2,1}$ and $S_{2,1}$ coefficients that contain an anomaly correlated with a failure
 265 of the accelerometers. We choose to replace these two coefficients with the SLR solution
 266 from Cheng et al. (2011) after October 2016. These replacements are not included in the
 267 CNES solution because it already includes SLR data at low degrees. Geocenter coefficients
 268 $C_{1,0}$, $C_{1,1}$ and $S_{1,1}$ are not included in our data and are set to 0 for the CNES solution
 269 where they come from SLR.

270 Previous studies provided estimates of the uncertainty of GRACE products from
 271 different centers, but not at large spatial and inter-annual time scales. For example, Kvas
 272 et al. (2019) compared the GRAZ solution with those from CSR, GFZ and JPL in terms
 273 of temporal Root Mean Square (RMS) over a grid, quiet RMS time series and 161-day
 274 signal. Wang et al. (2021); Dobslaw et al. (2020) compared the estimations of global mean
 275 ocean mass and mean barystatic sea level with solutions from different centers. Blazquez
 276 et al. (2018) compared the trends of the global water budget components from 5 GRACE
 277 centers. It also estimated the uncertainties associated with the processing parameters,
 278 namely, the geocentre motions, $C_{2,0}$, filtering, leakage and GIA. Another estimation of
 279 the GRACE products uncertainty can be given by the RMS value over ocean but it has
 280 not been proposed, yet, for inter-annual time scales (Chen et al., 2021). It is also worth
 281 noting that MASCON products can be useful in error assessment (Loomis et al., 2019b).
 282 In the following, we compare GIA, hydrology and non-tidal oceanic models.

283 **3.3 Glacial Isostatic Adjustment (GIA)**

284 The GIA signal induces linear trends in the gravity field variations. Effects of the
 285 post-glacial rebound are apparent in Antarctica, Northern America and Scandinavia. This

286 signal rectification uses GIA models based on global ice-loading history and mantle viscosity.
 287 We do not consider regional GIA models since they would give spurious estimates of the
 288 GIA signal out of the specific regions for which they have been designed (Whitehouse
 289 et al., 2012). Present-day ice melting is not taken into account in the post-glacial rebound
 290 models, it hence constitutes another source of uncertainty.

291 We compare three different global GIA models, namely A13 (Geruo et al., 2013),
 292 ICE-6G_D (VM5a) (Peltier et al., 2015, 2018) and Caron18 (Caron et al., 2018).

293 A13 is based on the ICE5G ice-loading history model (Peltier, 2004) and on the
 294 multilayered viscosity profile VM2 (Peltier, 2004). A13 is computed via a 3-D finite-element
 295 method that creates a 3-D viscosity structure. ICE-6G_D (VM5a) uses an update of ICE5G
 296 ice-load history with the addition of GNSS vertical rates constraints and Antarctica ice
 297 height change data (Argus et al., 2014). ICE-6G_D (VM5a) includes a more recent viscosity
 298 profile VM5a. Caron18 represents the mean of an ensemble of 128,000 forward models
 299 calculated in a Bayesian framework. For each run model, the viscosity structure and the
 300 scaling coefficients for the ice-load history of the Australian National University (ANU)
 301 model (Lambeck et al., 2010, 2014) vary. The final Caron18 GIA is a weighting of each
 302 model inferred by the probabilistic information and contains an estimate of the uncertainty
 303 from the dispersion between the models. A synthesis of these models is available in Table 3.

Table 3: Main characteristics of the GIA models

| Model | Ice History | Viscosity Model (VM) | Lateral Heterogeneity | GNSS data |
|----------|-------------|----------------------|-----------------------|-----------|
| A13 | ICE5G | VM2 | Yes | No |
| ICE-6G_D | ICE6G | VM5a | No | Yes |
| Caron18 | From ANU | Bayesian mean VM | No | Yes |

304 Comparisons between these three GIA models already exist, mainly with regard
 305 to the uplift rates as measured by GNSS and the viscosity profiles. Argus et al. (2014)
 306 and Peltier et al. (2015) compare ICE-6G_D with A13 respectively on Antarctica and
 307 North America. Caron et al. (2018) and Argus et al. (2021) compare ICE-6G_D with Caron18

308 on North America. It is worth noting that the closest model to the measured GNSS uplift
309 rate is ICE-6G_D.

310 Global GIA models are not associated with any uncertainty except for Caron18 and
311 studies rarely discuss that point (Caron et al., 2018; Melini & Spada, 2019). A way of
312 estimating the impact of the uncertainty of those models is by comparing some of them
313 for a specific application. Śliwińska et al. (2021) used two different GIA models to estimate
314 polar motion while Blazquez et al. (2018) compared three GIA models for the determination
315 of global ocean mass change and sea level budget. In the case of regional applications,
316 Kappelsberger et al. (2021) compared three global and two regional models with the uplift
317 estimation from GNSS on the north-east of Greenland. However, to the best of our knowledge,
318 there is no comparative study of GIA models based on the SH approach that was published,
319 and more specifically, on low SH degrees.

320 **3.4 Hydrology**

321 We compare five global hydrological models, namely the Global Land Data Assimilation
322 System Noah 2.1 (GLDAS) (Rodell et al., 2004), ERA5 (Hersbach et al., 2020), WaterGAP
323 Global Hydrology Model version 2.2d (WGHM) (Döll et al., 2003), Interaction Sol-Biosphère-
324 Atmosphère CNRM version of TRIP (ISBA-CTRIP, further referred to as ISBA) (Decharme
325 et al., 2019) and Hydrological Land Surface Discharge Model (LSDM) (Dill, 2008). Hydrological
326 models contain mainly annual and semi-annual signals. With the temporal and spatial
327 filtering to access the core-like scales, the residuals studied are small compared to the
328 original signals. For example, the RMS value of ISBA over continent is 3.64 cm in EWH
329 and 1.47 cm EWH after temporal filtering. These residuals contain climatic modes like
330 El Niño-Southern Oscillation.

331 The five hydrological models considered solve the vertical water mass balance but
332 only three of them also solve the lateral fluxes. The water mass balance is expressed as
333 the Terrestrial Water Storage (TWS) anomaly.

334 For GLDAS, the permanently ice-covered areas have been masked out. GLDAS has
335 a spatial resolution of 0.25° per 0.25° and a temporal resolution of 3 hours. ERA5 has
336 the same temporal and spatial resolutions. ERA5 is the new global model from Copernicus
337 Climate Change Service that replaces the ERA-Interim reanalysis (Dee et al., 2011). GLDAS
338 uses Global Precipitation Climatology Centre (GPCC) V1.3 Daily Analysis (Adler et al.,

339 2003) has precipitation model. GPCC is a family of precipitation models based on in situ
 340 raingauge data to estimate monthly precipitation. For these two models, gravitational
 341 potential changes induced by hydrological mass redistribution and loading are computed
 342 as detailed in Petrov and Boy (2004) and Gégout et al. (2010).

343 WGHM, ISBA and LSDM are also supplemented with lateral fluxes solving. We
 344 use the variant IRR100 of WGHM forced with GPCC monthly V7.0 precipitation (Schneider
 345 et al., 2016). The output of the WGHM that we use in this study was already at a monthly-
 346 averaged temporal scale and the spatial resolution is 0.5° . ISBA-CTRIP is the combination
 347 of a water balance model (ISBA) with a runoff model (CTRIP). ISBA has a temporal
 348 resolution of 3 hours and a spatial resolution of 1° and it also uses GPCC V6 as a precipitation
 349 model. LSDM has a daily temporal frequency and a spatial resolution of 1° . LSDM has
 350 been designed for large spatial scale geodetic applications such as the study of Earth’s
 351 polar motion (Dill et al., 2010; Jin et al., 2012). Among the three models, only WGHM
 352 includes human-induced effects of freshwater resources. This contribution is extremely
 353 important when accounting for the contribution of freshwater fluxes to the global ocean
 354 (Schmied et al., 2020).

Table 4: Characteristics of the hydrological models

| Acronym | Precipitation model | Sampling period | Space resolution |
|---------|-------------------------|-----------------|------------------|
| ERA5 | Simultaneously generate | 1 h | 0.25° |
| GLDAS | GPCP | 3 h | 0.25° |
| ISBA | GPCC | 3 h | 1° |
| WGHM | GPCC | monthly average | 0.5° |
| LSDM | ECMWF | daily | 1° |

355 Each models has been resampled to a monthly time scale with an average over the
 356 month. The time coverage of comparison goes from 2002 to the end of 2016, this corresponds
 357 to the end of the WGHM model provided to us.

358 Previous studies compared hydrological models with GRACE gravity field variations
 359 but not with this diversity of models and not at these inter-annual and large spatial scales

360 (Lenczuk et al., 2020; Jin & Feng, 2013; Liu et al., 2019). At inter-annual and decadal
361 scales, hydrological models compared with GRACE solution are underestimating the hydrological
362 signal on river basins and regarding climate modes (Scanlon et al., 2018; Pfeffer et al.,
363 2021, 2022).

364 **3.5 Non-tidal oceanic loading**

365 We compare three oceanic loading models, namely Ocean Model for Circulation
366 and Tides (OMCT) (Dobslaw et al., 2013), Max-Planck-Institute for Meteorology Ocean
367 Model (MPIOM) (Jungclaus et al., 2013) and Toulouse Unstructured Grid Ocean model
368 (T-UGOm) (Carrere & Lyard, 2003). These models are used in GRACE solutions to correct
369 for oceanic loading effects. For official centers, these models correspond to the GAB solution
370 that contains the contribution of the dynamic ocean to ocean bottom pressure. OMCT
371 has been used by official GRACE centers between Releases 1 and 5. MPIOM is used for
372 the Release 6. T-UGOm is used by the CNES for the correction of the GRACE data (and
373 not for GRACE-FO).

374 OMCT and MPIOM are baroclinic ocean models with a spatial resolution of 1° .
375 They are adjustments from another model, the climatological Hamburg Ocean Primitive
376 Equation (HOPE) model. They are forced by external information from the operational
377 analyses of the European Centre for Medium-Range Weather Forecast (ECMWF). They
378 compute water elevations, three-dimensional horizontal velocities, potential temperature
379 and salinity. Both MPIOM and OMCT are forced by surface winds, pressure, atmospheric
380 freshwater fluxes and surface temperature. MPIOM is using river runoff, sea-ice and corrects
381 for the inverted barometer response of the oceans as opposed to OMCT. The T-UGOm
382 barotropic ocean model is based on an unstructured grid with a higher resolution on coastal
383 area. It does not represent variations of temperature and salinity but only displacement
384 of the barotropic fluid. T-UGOm is using wind and atmospheric pressure forcing from
385 ERA-interim and does not correct the inverted barometer response. Temporal and spatial
386 resolutions of each model are detailed in Table 5.

387 To compare these three models we can not use the GAB solutions from GRACE
388 releases because of the difference in the correction of the inverted barometer effect. The
389 GAB solution for AOD1B RL06 with MPIOM uses the correction of the inverted barometer
390 effect. It implies that the AOD1B RL06 GAA solution, which corresponds to the atmospheric

Table 5: Characteristics of the ocean models

| Acronym | Sampling period | Spatial resolution | Inverted barometer |
|---------|-----------------|--------------------|--------------------|
| OMCT | 90 min | 1° | No |
| MPIOM | 20 min | 1° | Yes |
| T-UGOm | 3 hours | unstructured grid | No |

loading effect, is equal to a constant value over oceanic area. For OMCT and T-UGOm, the GAB solution contains the inverted barometer effect and the GAA solution does not contain the inverted barometer effect. Regarding this, we compare the GAC solutions which are in fact the sum of the GAB (ocean loading) and the GAA (atmospheric loading) solutions over the ocean. This sum over oceanic areas corresponds to the oceanic bottom pressure and is given by the GAD solution in GRACE releases. To compare these oceanic loading models, the best way is to use the related GAD solutions.

Previous studies compared these models but at sub-monthly time scales (Bonin & Save, 2019; Dobslaw et al., 2015). To our knowledge, there are no comparative studies of ocean loading models on inter-annual and decadal temporal scales. Schindelegger et al. (2021) also compared some other oceanic models with MPIOM at sub-monthly time scales. We did not include these other models because some are in-house products and other are GRACE-dependent.

4 Comparison of gravity field solutions and models

In our approach, we cannot directly estimate the accuracy of solutions and models. We use an ensemble approach where the dispersion between solutions and models provides an estimate of the uncertainty. This estimate is a first lower bound that does not take into account any bias. This approach is similar to Blazquez et al. (2018) or Marti et al. (2022).

Comparisons between solutions and models are quantified as the Root Mean Square (RMS) difference between both objects weighted by latitude. In order to compute the weighted RMS, solutions and models are projected on a grid of $0.5^\circ \times 0.5^\circ$ degree and we compute the difference between the grids.

414 **4.1 Differences between GRACE solutions**415 **4.1.1 GRACE analysis centers**

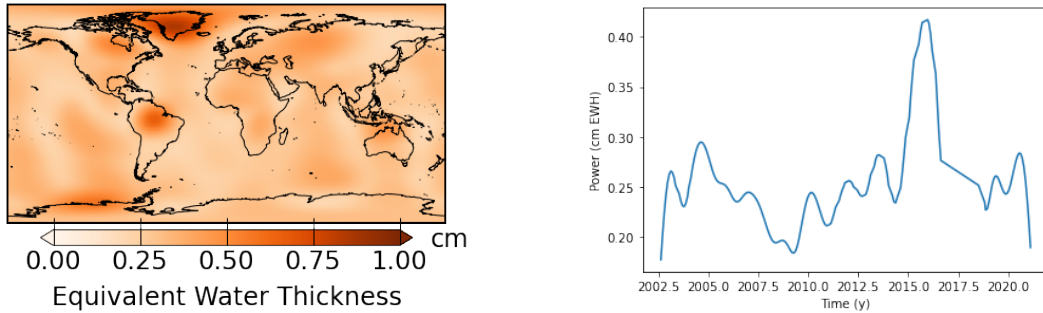
416 Comparison between GRACE solutions requires to minimize side effects due to the
 417 temporal filtering. We hence remove the first and last three months of the solutions.

| | JPL | GFZ | GRAZ | CNES | COSTG | RMS |
|-------|------|------|------|------|-------|------|
| CSR | 0.17 | 0.35 | 0.32 | 0.45 | 0.16 | 1.82 |
| JPL | | 0.32 | 0.31 | 0.45 | 0.16 | 1.81 |
| GFZ | | | 0.45 | 0.53 | 0.30 | 1.82 |
| GRAZ | | | | 0.45 | 0.27 | 1.87 |
| CNES | | | | | 0.42 | 1.86 |
| COSTG | | | | | | 1.81 |

Table 6: RMS differences in cm EWH between different GRACE solutions and RMS value of each model after spatial and temporal filtering

418 Table 6 contains the RMS differences in cm EWH between the spatially and temporally
 419 filtered GRACE solutions from different analysis centers. For reference, the RMS value
 420 of the CSR solution is 1.82 cm EWH. The first group, CSR, JPL and COST-G solutions,
 421 is the most similar with an RMS difference of 0.16-0.17 cm EWH or 9% of the original
 422 RMS value for one solution. There is an increase of the difference to 0.22 cm EWH in
 423 2016 at the end of GRACE lifespan corresponding to the accelerometer failure of one of
 424 the two satellites. Then comes a second group with GFZ and GRAZ which have an RMS
 425 difference of 0.3 cm EWH with the first group or 17% of the original RMS value for one
 426 solution. But the difference of these two solutions with the first group is different according
 427 to the considered epoch. GFZ has a peak going up to 0.7 cm EWH at the end of the GRACE
 428 lifespan. For GRAZ, in this temporal period, the difference goes up to 0.5 cm EWH but
 429 then it goes to 0.7 cm EWH at the end of the GRACE-FO time series. For the GFZ, the
 430 spatial distribution of differences corresponds to a global noise without any specific pattern.
 431 But for the GRAZ solutions, differences are located in areas of large signals, in the Amazon
 432 basin and Greenland. The CNES solution has a RMS difference of 0.45 cm EWH (25%

433 of the original RMS value) with respect to other solutions with a temporal difference of
 434 1 cm EWH at the beginning of the GRACE mission and at the end of the GRACE life
 435 span. The spatial localisation of these differences are located in areas of strong hydrological
 436 signal like the Amazon basin and India. Figures to illustrate these analyses are available
 437 in Appendix A.



(a) Average of RMS differences in cm EWH
spatially represented

(b) Average of RMS differences in cm EWH
represented trough time

Figure 4: Average of RMS differences in cm EWH after spatial and temporal filtering

438 To continue the analysis of the differences between the GRACE solutions, it is important
 439 to consider the average RMS values over time and in different spatial areas (Fig. 4). The
 440 highest values over Greenland, Antarctica and Amazonia correspond spatially to areas
 441 with strong inter-annual signals. Thus, the stronger the signal, the larger the differences
 442 between the solutions. For the temporal variations of the RMS differences between solutions,
 443 the difference are twice larger at the end of the GRACE mission. The degradation of the
 444 quality of GRACE solutions is well known and has already been documented (Kvas et
 445 al., 2019; Dahle et al., 2019). This degradation is due to the failure of the accelerometer
 446 after November 2016 and is smoothed trough time in Figure 4b because of the temporal
 447 filtering. Otherwise, the RMS values over time are about 0.25 cm in EWH.

448 **4.1.2 GIA models**

449 Figure 5 represents the difference in rate of EWH in mm per year between the models
 450 with a spatial resolution of 2400 km after a truncation at degree 60 and the application
 451 of a Gaussian filter. In Appendix B, the same figure without spatial filtering is available.

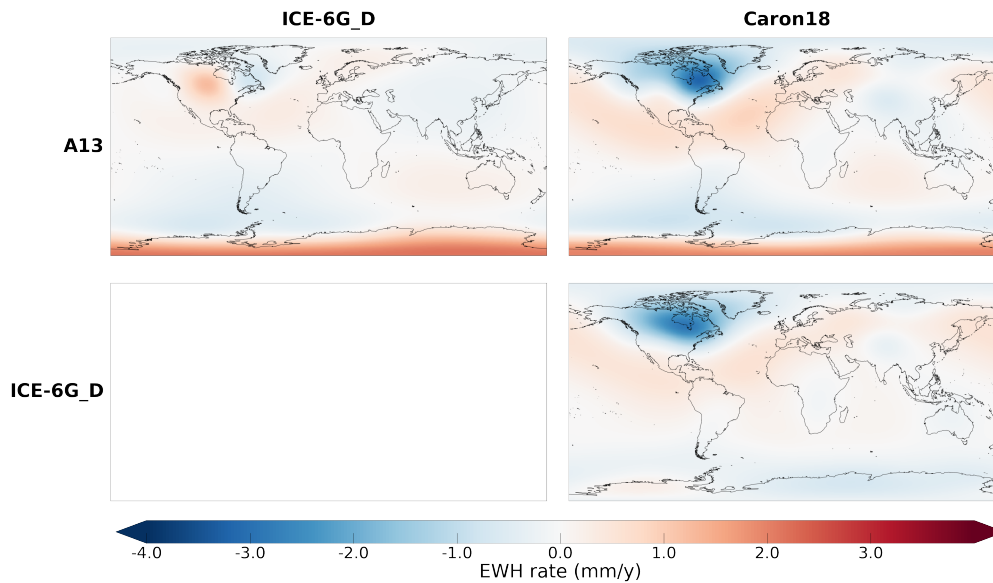


Figure 5: Difference between GIA models spatially filtered in EWH rate (mm/y)

452 The models are similar in Scandinavia. The Caron18 model differs from the others
 453 in North America and the A13 model differs from the others in Antarctica. These two
 454 statements correspond to previous observations (Argus et al., 2021, 2014). There are small
 455 differences between A13 and the ICE-6G_D model in North America (± 1 mm/y in EWH)
 456 compared to those in Antarctica (± 3 mm/y). Peltier et al. (2015) pointed out a larger
 457 difference on the western and eastern sides of Hudson Bay in Canada that we recovered
 458 without the spatial filtering (Appendix B). However, in Figure 5, the spatial filtering reduces
 459 these differences, one being negative and the other positive, they counterbalance each
 460 other.

461 In North America, the disagreement between models goes up to 6 mm in EWH per
 462 year. In Antarctica, the differences between models are up to 10 mm in EWH per year.
 463 These differences in velocity are currently accumulated over 20 years and at the time of
 464 publication of this article, they lead to a potential error of 12 cm in EWH per year over
 465 North America and of 20 cm in EWH per year over Antarctica.

466 *4.1.3 Hydrological models*

467 Table 7 contains the RMS differences in cm EWH between spatially and temporally
 468 filtered hydrological loading models (Newtonian attraction and mass redistribution associated

| | GLDAS | ISBA | WGHM | LSDM | RMS |
|-------|-------------|-------------|-------------|-------------|-------------|
| ERA5 | 0.89 | 0.89 | 1.36 | 1.50 | 0.91 |
| GLDAS | | 0.89 | 1.20 | 1.74 | 1.26 |
| ISBA | | | 1.13 | 1.56 | 1.00 |
| WGHM | | | | 2.10 | 1.36 |
| LSDM | | | | | 1.66 |

Table 7: RMS difference in cm EWH between hydrological models and RMS value of each model after spatial and temporal filtering over the continents

469 with elastic deformation) over continents without Greenland and Antarctica. The RMS
 470 difference goes from 0.89 to 2.10 cm EWH or 100% to 155% of the original RMS value
 471 for one model. For example, the RMS values of ISBA and LSDM are respectively 1.00
 472 and 1.66 cm EWH.

473 Because hydrological models take into account different processes, they yield very
 474 different TWS anomalies, leading to large differences in the predicted gravity variations
 475 at large spatial and temporal scales. At inter-annual and large spatial scales, ERA5, GLDAS
 476 and ISBA display relatively similar signals (Fig. 6a). Probably because it takes into account
 477 anthropogenic use of freshwater, WGHM exhibits larger differences, with larger TWS
 478 changes at inter-annual signals located in India and in the northern hemisphere than the
 479 other models (Fig. 6c).

480 LSDM shows the largest difference with other models. It has a very strong signal
 481 over the Nile area in North Africa (Fig. 6b). The difference between LSDM and other
 482 hydrological models like GLDAS has been documented and explained by the particular
 483 river channels redistribution of water (Dill & Dobslaw, 2013; Dill et al., 2018).

484 The same analysis has been done on hydrological loading model without spatial filtering
 485 in Appendix C1.

486 The quality of hydrological loading models is uneven. To evaluate this quality we
 487 look at the percentage of RMS explained by the models in the variation of the gravity
 488 field. We compare, over the continents, the RMS of the GRACE time series (COST-G)

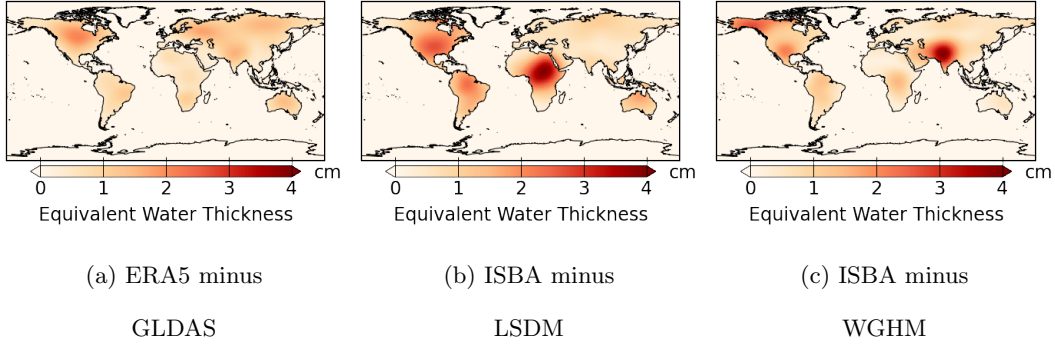


Figure 6: Maps of RMS difference between hydrological models over the continents after spatial and temporal filtering

489 with the RMS of GRACE minus a hydrological model. The variation of the RMS value
 490 gives the percentage of RMS explain by the model in the GRACE time series (Table 8)
 491 over non-glaciaded continents (Greenland and Antartica are not include).

| | ERA5 | GLDAS | ISBA | WGHM | LSDM |
|----------------|------|-------|------|------|------|
| Percentage (%) | 7 | 0 | 24 | 21 | -16 |

Table 8: Percentage of RMS explain by hydrological models in the GRACE time series at inter-annual scales with a spatial filtering over non-glaciaded continents

492 At inter-annual and large spatial scales, ISBA and WGHM reduce the variance of
 493 GRACE solutions by more than 20%. According to this criteria they have the best quality
 494 among the five models considered. ERA5 and GLDAS are close to 0% and LSDM is negative
 495 with -16%. It does not modelize gravity field variations in GRACE time-series and contains
 496 other signals. Global hydrological models struggle to explain GRACE data, likely due
 497 to inaccurate meteorological forcing, unresolved groundwater processes, anthropogenic
 498 influences, changing vegetation cover, limited calibration and validation datasets (Pfeffer
 499 et al., 2022).

| | MPIOM | T-UGOm | RMS |
|--------|-------------|-------------|-------------|
| OMCT | 0.33 | 0.45 | 0.42 |
| MPIOM | | 0.42 | 0.39 |
| T-UGOm | | | 0.44 |

Table 9: RMS difference in cm EWH between oceanic loading products and RMS value of each model after spatial and temporal filtering over the oceans

500 **4.1.4 Non-tidal oceanic loading models**

501 Table 9 contains the RMS differences in cm EWH between spatially and temporally
 502 filtered oceanic and atmospheric loading products over the oceans. The RMS difference
 503 goes from 0.33 to 0.45 cm EWH between models or 79% to 107% of the original RMS
 504 value for one model. For comparison, the RMS value for OMCT is 0.42 cm EWH. Because
 505 oceanic loading models come from different climate and fluid mechanics models, they have
 506 a very different spatial and temporal content, leading to large differences. Differences
 507 are mostly located in Arctic and Antarctic areas, coastal regions and in the Antarctic
 508 Circumpolar Current area (Fig. 7). OMCT has more signal in the Arctic while MPIOM
 509 and T-UGOm have more signal near Antarctica in the Ross Sea (Fig. 7).

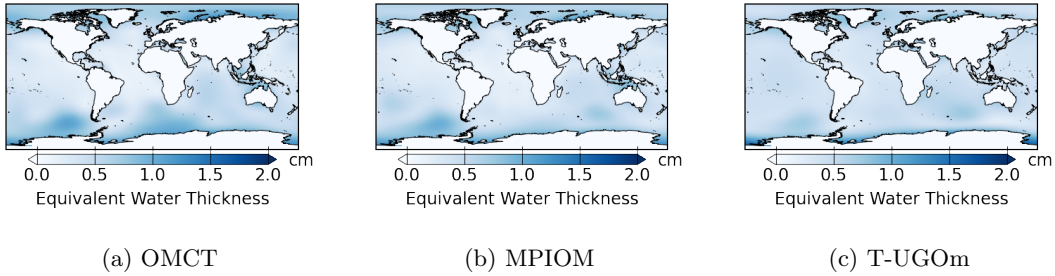


Figure 7: Maps of RMS for oceanic loading products after spatial and temporal filtering over the oceans

510 There is another difference between these models: they are monthly products with
 511 potential missing days each month. These missing days correspond to low quality data

512 but may vary between models and releases. This is the case for months at the beginning
 513 and at the end of the GRACE mission in 2002 and between 2012 and 2017. For example,
 514 for the month of August 2016, the MPIOM products from official centers contain measurements
 515 from days of year 221 to 247 while the T-UGOm products from the CNES contain measurements
 516 from days of year 214 to 244.

517 The same analysis has been done for oceanic loading models without spatial filtering
 518 (Appendix D1).

519 **4.2 Impact of geophysical corrections on Stokes coefficients**

520 We have quantified the uncertainties of GRACE solutions and correction models
 521 in terms of RMS of the differences over grids. Another interesting approach is to look
 522 at SH coefficients. Core processes signal might be present from degree 2 onward to higher
 523 degrees with decreasing amplitudes.

524 To estimate the impact of an error in a model on specific SH coefficients, we have
 525 performed some synthetic test. An artificial synthetic signal is added to the GRACE gravity
 526 data on a bounded area. We choose these synthetic signals with regard to the observed
 527 errors in the GIA and hydrological loading models. We study the effects of this synthetic
 528 signal on the retrieved Stokes coefficients in terms of RMS value. To compare with the
 529 time-variable gravity measured by GRACE, we normalized each SH coefficients by the
 530 standard deviation $\sigma_{l,m}^{GRACE}$ of the degree- l , order- m Stokes coefficient from the COST-
 531 G solution. We note $I_{l,m}$ the normalized RMS value of the coefficient of degree l and order
 532 m given by:

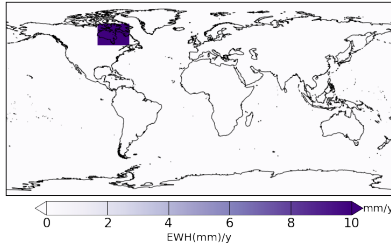
$$I_{l,m} = \frac{\sqrt{\frac{1}{n} \sum_t \Delta C_{l,m}(t)^2}}{\sigma_{l,m}^{GRACE}} \quad (8)$$

533 With t the index of the time vector. This representation gives an estimate of the contamination
 534 by an error on the correction model with respect to the corrected GRACE signal.

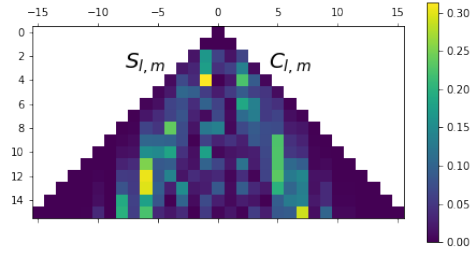
535 **4.2.1 Impact of an error in the GIA model**

536 To study the effect of adding a fiducial GIA rectification, we create three synthetic
 537 signals corresponding to errors seen in 4.1.2.

- 538 • A linear signal of 10 mm/y in EWH located in North America with latitude between
- 539 50° and 70° and longitude between −95° and −65°.
- 540 • A linear signal of 6 mm/y in EWH located in Antarctica with latitude under −80°.
- 541 • A linear signal of 3 mm/y in EWH located in Antarctica with latitude under −70°
- 542 and longitude between −160° and −30°.



(a) Synthetic signal in North America in EWH



(b) SH power normalized by GRACE standard deviation up to degree 15

Figure 8: Effect of a 10 mm/yr trend in North America in the GIA model (a) on GRACE SH coefficients (b).

543 Introducing a 10 mm/y trend in North America alters the SH coefficients (Fig. 8).
 544 The error created on the GRACE $S_{4,1}$ coefficient by this fiducial reduction might be up
 545 to 30%. The other two synthetic experiments, with a trend at lower latitudes, affect the
 546 coefficients of orders 0 and 1 (Appendix E). The largest effect for a trend of 6 mm/y over
 547 Antarctica center is on $C_{8,0}$ with a trended bias of 50% of the GRACE RMS value. For
 548 a 3 mm/y trend in Antarctica between −160° and −30° in longitude, the effects are smaller
 549 with 15% of the GRACE RMS value on $S_{6,1}$ and $S_{8,1}$ (Appendix E).

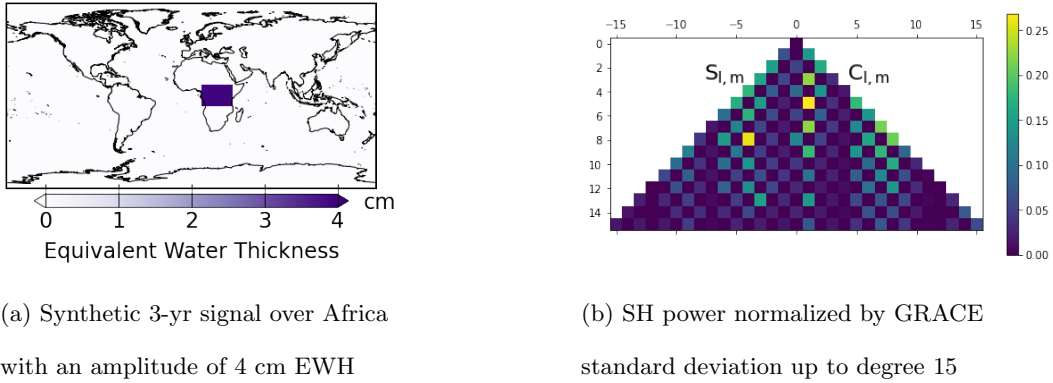
550 4.2.2 Hydrology

551 Three cases have been simulated with a sinusoidal signal of period 3 years. They
 552 correspond to the difference between hydrological models established in Figure 6 over
 553 large hydrological basins:

- 554 • A sinusoidal signal of 4 cm in EWH over Africa (latitude between −10° and 10°,
 555 longitude between 10° and 35°).

- 556 • A sinusoidal signal of 3 cm in EWH over Amazonia (latitude between 0° and 20° ,
- 557 longitude between -70° and -40°).
- 558 • A sinusoidal signal of 4 cm in EWH over India (latitude between 20° and 30° , longitude
- 559 between 70° and 90°).

560 The 3-year period was chosen arbitrarily and represents a residual hydrological signal.



(a) Synthetic 3-yr signal over Africa with an amplitude of 4 cm EWH

(b) SH power normalized by GRACE standard deviation up to degree 15

Figure 9: Effect of a sinusoidal signal over Africa (a) on GRACE SH coefficients (b)

561 A 4-cm sinusoidal signal over Africa affects $C_{5,1}$ and $S_{8,4}$ by an amount of 25% of
 562 the GRACE RMS value (Fig. 9). A 3 cm sinusoidal signal over Amazonia affects $C_{4,3}$
 563 and $S_{2,2}$ by an amount of 20%, while a 4 cm signal over India affects $C_{8,7}$ and $S_{8,6}$ by
 564 an amount of 10% (Appendix F).

565 5 Discussions & Conclusions

566 In this paper, we firstly addressed different core processes that can create gravity
 567 variation and estimated their amplitudes. Then, we presented different GRACE SH solutions,
 568 GIA and loading models. We compared each family of products with respect to the differences
 569 in RMS or trend at large spatial and inter-annual time scales. From this, we estimated
 570 their uncertainties and the associated SH uncertainties.

571 A summary of the orders of magnitude of predicted core signals and of the dispersion
 572 between the different solutions and models obtained in this article is given in Table 10.
 573 It contains the amplitude of the RMS difference at degrees 2, 6 and 10. The largest core
 574 signals amplitude with regard to the uncertainty is found at degree 2. At degrees 6 and

| Type of data | (cm EWH) | Amplitude (cm EWH) | | |
|---------------------------------------|---------------------|--------------------|----------|-----------|
| | Mean RMS difference | Degree 2 | Degree 6 | Degree 10 |
| Maximum of the estimated core signals | 0.5 | 0.5 | 0.04 | 0.004 |
| GRACE solutions | 0.34 | X | 0.1 | 0.04 |
| Hydrological loading models | 1.32 | 0.37 | 0.38 | 0.41 |
| Oceanic loading models | 0.40 | 0.16 | 0.08 | 0.03 |

Table 10: Amplitude of core estimated signals compared to RMS difference between products at inter-annual and large spatial scales and at degrees 2, 6 and 10

575 10, the amplitude estimated from core signals is an order of magnitude smaller than the
576 estimated uncertainty of the GRACE solutions. To summarize the information on amplitude
577 from this table:

- 578 • Mass variations from the core are characterized by their low degree signature and
579 by an inter-annual / decadal time scale. The maximal amplitude of core effects
580 is evaluated at 0.5 cm EWH which is slightly larger than the estimated GRACE
581 uncertainty at inter-annual and large spatial scales.
- 582 • GRACE solutions are in good agreement with a dispersion that represents some
583 10 to 20% of the total signal, however, the agreement is not the same over the time
584 span covered by the two missions, with difference mainly at the beginning and end
585 of each.
- 586 • For hydrological loading models, the agreement is uneven (see also Fig. 6 & Table
587 7, 8). The dispersion between models is as large as the RMS value of models themselves.
588 However, ISBA and WGHM are closer to GRACE solutions.
- 589 • For the oceanic loading models, the agreement is generally poor (see also Fig. 7).
590 For each model, high-intensity signals are spatially located in different areas at
591 inter-annual time scales. For example, T-UGOm is the only model to report large
592 oceanic mass variations under South Africa.
- 593 • The GIA effects are not included in this recapitulating table as they are localized
594 in specific areas: North America, Greenland and Antarctica. To remind, GIA-mismodelled

595 linear effects can go up to a 20 cm EWH after 20 years over North America. GIA
596 errors will only impact the trend and not the inter-annual signals.

597 When models characterising surface processes are considered to minimise the signature
598 of these processes in the gravity data, they might indeed create some spurious signals
599 on some areas. This would also create a spurious signal on specific SH (Fig. 8, Fig. 9)
600 up to 50% of the total signal on inter-annual time scale.

601 The estimated maximum amplitude of core signals based on a literature review is
602 5 mm in EWH at the Earth's surface. Core mass variations are most significant on decadal
603 time scales and at low degrees. In this context, it is relevant to analyse the Earth's gravity
604 products from GRACE and loading models through these specific scales. The RMS difference
605 between GRACE solutions of 3.4 mm in EWH shows how difficult is to detect potential
606 core signals. This difficulty is somehow reinforced when considering the use of loading
607 models to minimize these components in the gravity signal, as the differences between
608 loading products are large and these products are not completely adapted to our purpose.

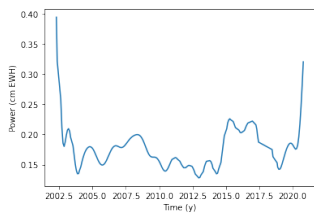
609 A careful analysis of the time-variable gravity field data needs to be done for detecting
610 signals from the core processes. Firstly, the data-gap between GRACE and GRACE-FO
611 should be filled to ensure continuity and to improve the products quality (Richter et al.,
612 2021). The largest signals in GRACE-kind solutions are due to the Earth's surface processes.
613 The inter-annual variability analysis through climate modes (Pfeffer et al., 2021) needs
614 also to be considered. In order to detect tiny signals related to the core more sophisticated
615 methods are needed such as empirical orthogonal function analysis (Schmeer et al., 2012)
616 or independent component analysis (Frappart et al., 2011). Recently, (Saraswati et al.,
617 2022) applied Singular Value Decomposition (SVD), Principal Component Analysis (PCA)
618 and Multivariate Singular Spectrum Analysis (MSSA) to separate distinct spatio-temporal
619 patterns in magnetic and gravity field. Moreover, synthetic tests have to be performed
620 to evaluate the sensitivity of these methods with respect of the Earth's core signals.

621 Both gravity and magnetic fields are complex, with a wide range of temporal and
622 spatial variations and to describe them new models are needed. Only by modelling and
623 interpreting multiple data sets a multifaceted image of the true structure of the Earth
624 can be obtained.

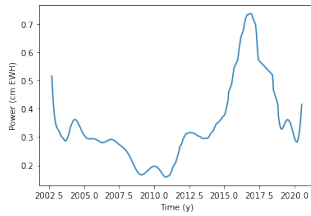
625
626
627

6 Supplementary materials

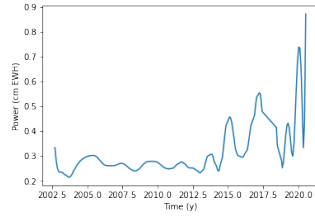
Appendix A Temporal variation of the RMS difference between various GRACE solutions



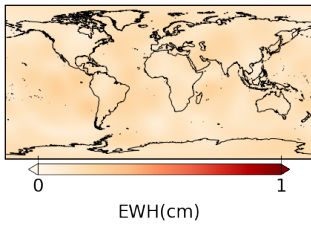
(a) Temporal RMS difference between CSR and JPL solutions



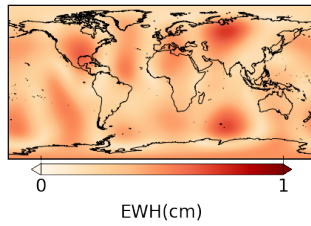
(b) Temporal RMS difference between CSR and GFZ solutions



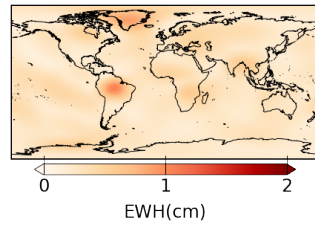
(c) Temporal RMS difference between CSR and GRAZ solutions



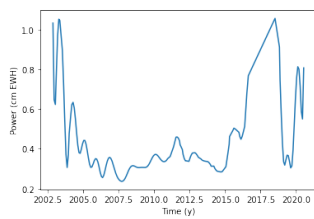
(d) Spatial RMS difference between CSR and JPL solutions



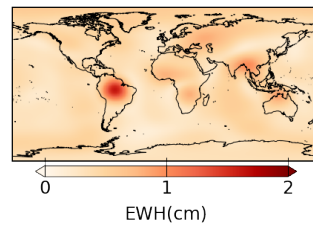
(e) Spatial RMS difference between CSR and GFZ solutions



(f) Spatial RMS difference between CSR and GRAZ solutions



(g) Temporal RMS difference between CSR and CNES solutions



(h) Spatial RMS difference between CSR and CNES solutions

Figure A1: RMS difference between GRACE center solutions on temporal and spatial representation

628

Appendix B Difference between GIA models without spatial filtering

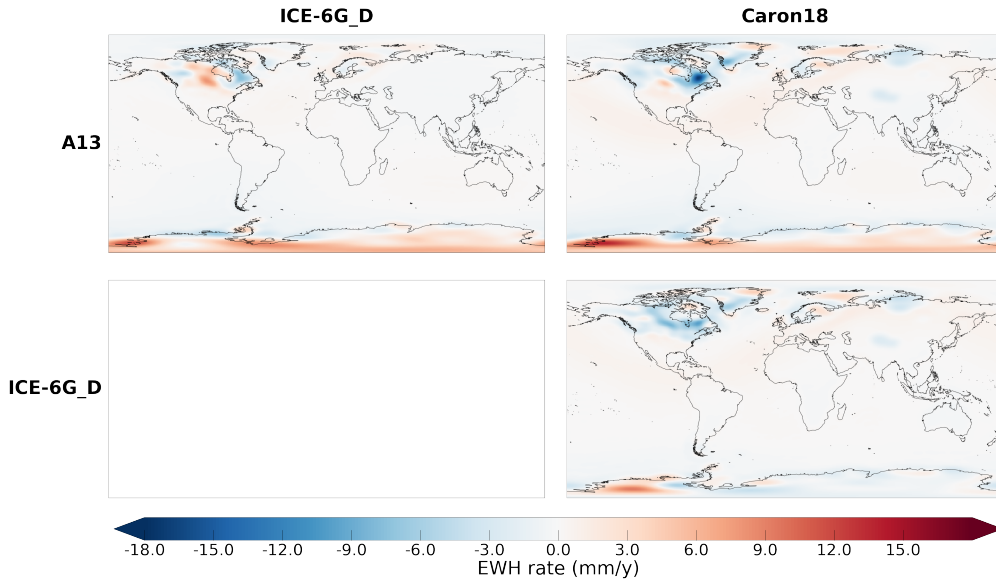


Figure B1: Difference of between GIA models in EWH rate (mm/y)

629

The amplitude of the GIA signal is five times larger without spatial filtering and the signal is more localize.

630

631

Appendix C Difference between hydrological loading with temporal filtering and without spatial filtering

632

| | GLDAS | ISBA | WGHM | LSDM | RMS |
|-------|-------|------|------|------|------|
| ERA5 | 2.06 | 2.11 | 2.92 | 2.69 | 2.35 |
| GLDAS | | 2.04 | 2.74 | 2.99 | 2.67 |
| ISBA | | | 2.55 | 2.66 | 2.43 |
| WGHM | | | | 3.67 | 3.05 |
| LSDM | | | | | 2.47 |

Table C1: RMS difference in cm EWH between hydrological models and RMS value of each model after a temporal filtering

633 Table C1 contains the RMS difference in cm EWH between temporally filtered hydrological
 634 models over continents without Greenland and Antarctica. The RMS difference goes from
 635 2.04 to 3.67 cm EWH between models. For example of comparison, the RMS value of
 636 ISBA and WGHM are respectively 2.43 and 3.05 cm EWH.

637 At inter-annual time scales, the models show different signals. For example, WGHM
 638 is the only one to contain a strong signal over India and North America, while LSDM
 639 is the only one to contain a signal over the Nile region in Africa. They do not correspond
 640 at all.

641 We can also note that the spatial filtering smooths the signal amplitude.

642 Appendix D Difference between oceanic loading with temporal filtering 643 and without spatial filtering

| | MPIOM | T-UGOm | RMS |
|--------|-------|--------|------|
| OMCT | 0.72 | 0.79 | 0.84 |
| MPIOM | | 0.74 | 0.77 |
| T-UGOm | | | 0.52 |

Table D1: RMS difference in cm EWH between oceanic loading solutions and RMS value of each model after temporal filtering

644 Table D1 contains the RMS difference in cm EWH between temporally filtered oceanic
 645 and atmospheric loading models over the oceans. The RMS difference goes from 0.72 to
 646 0.79 cm EWH between models. For comparison, the RMS value for OMCT is 0.84 cm
 647 EWH. This means that models are not in agreement at inter-annual scales and they represent
 648 very different signals.

649

Appendix E Cases $n^{\circ}2$ and $n^{\circ}3$ for GIA synthetic error effects

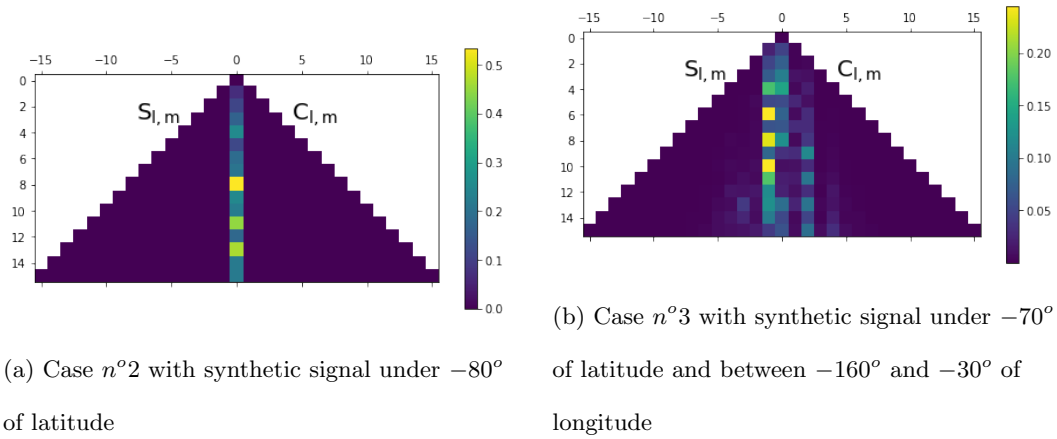


Figure E1: SH power normalized by GRACE standard deviation up to degree 15

650

Appendix F Cases $n^{\circ}2$ and $n^{\circ}3$ for synthetic error effects corresponding to hydrological loading

651

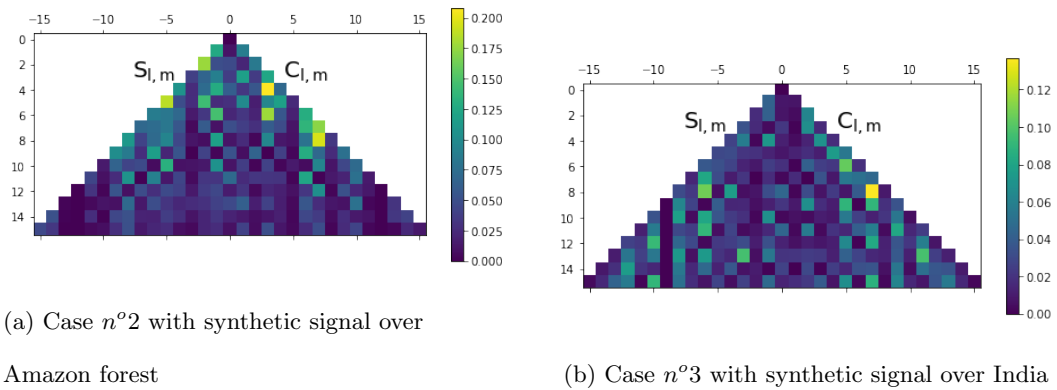


Figure F1: SH power normalized by GRACE standard deviation up to degree 15

652

Acronyms

653

AIUB Astronomical Institute University Bern

654

CMB Core-Mantle Boundary

655

CNES Centre national d'études spatiales

656

CSR Center for Space Research

657 **EWH** Equivalent Water Height
658 **GFZ** German Research Centre for Geosciences
659 **GIA** Glacial Isostatic Adjustment
660 **GLDAS** Global Land Data Assimilation System
661 **GRACE** Gravity Recovery And Climate Experiment
662 **GRACE-FO** Gravity Recovery And Climate Experiment Follow-On
663 **GSM** GRACE Satellite-only Model
664 **IFG TU Graz** Institute of Geodesy at Graz University of Technology
665 **ISBA** Interaction Sol-Biosphère-Atmosphère
666 **ISBA-CTrip** Interaction Sol-Biosphère-Atmosphère CNRM version of TRIP
667 **JPL** Jet Propulsion Laboratory
668 **MPIOM** Max-Planck-Institute for Meteorology Ocean Model
669 **OMCT** Ocean Model for Circulation and Tides
670 **RMS** Root Mean Square
671 **SH** Spherical Harmonics
672 **SLR** Satellite Laser Ranging
673 **T-UGOm** Toulouse Unstructured Grid Ocean model
674 **TWS** Total Water Storage
675 **WGHM** WaterGAP Global Hydrology Model

676 **Acknowledgments**

677 This work is supported by the Centre national d'études spatiales (CNES) and by the Doctoral
678 School Earth and Environmental Sciences (ED 413) of the University of Strasbourg in
679 the Institut Terre et Environnement de Strasbourg (ITES, CNRS UMR7063). This project
680 has received funding from the European Research Council (ERC) under the European
681 Union's Horizon 2020 research and innovation program (GRACEFUL Synergy Grant agreement
682 No 855677).

683 Love numbers and $\kappa(r)$ values to estimate Earth's core signals have been kindly
684 provided by Mathieu Dumberry, we thank him for these inputs.

685 We thank the editor Paul Tregoning and the two referees for their valuable remarks
686 which improved the first manuscript.

687 GRACE and GRACE-FO missions are sponsored by the National Aeronautics and
 688 Space Administration and the Deutsches Zentrum für Luft-und Raumfahrt. GRACE and
 689 GRACE-FO Level-2 temporal solutions were obtained from the PO.DAAC Drive for CSR,
 690 GFZ and JPL centers, from <https://icgem.gfz-potsdam.de/> for ITSG center, from
 691 <https://grace.obs-mip.fr/> for CNES center and from [https://icgem.gfz-potsdam](https://icgem.gfz-potsdam.de/)
 692 [.de/](https://icgem.gfz-potsdam.de/) for the COST-G combination. The GIA models were obtained from the PO.DAAC
 693 Drive (<http://grace.jpl.nasa.gov>). Time-variable gravity field coefficients due to hydrological
 694 loading can be downloaded from EOST loading service (<http://loading.u-strasbg.fr/>)
 695 for ERA5 and GLDAS models. LSDM model is available on the ESMGFZ Product repository
 696 (<http://rz-vm115.gfz-potsdam.de:8080>) and is produced by IERS Associated Product
 697 Centre Deutsches GeoForschungsZentrum GFZ Potsdam. The ISBA-CTRIP model made
 698 by the "Centre National de Recherches Météorologiques" (CNRM) of Météo-France has
 699 been provided by Bertrand Descharmes. The WGHM model (<http://www.watergap.de/>)
 700 has been provided by Denise Caceres from Frankfurt University. MPIOM and OMCT
 701 are available on the PO.DAAC Drive and T-UGOm model has been provided by the CNES.

702 Finally, the Python 3.8 code used for this publication is based on a Github project
 703 by Tyler Tsutterley (<https://github.com/tsutterley/read-GRACE-harmonics>). The
 704 adapted version can be found on <https://github.com/hulecom/read-GRACE-harmonics>
 705 repository.

706 References

- 707 Adhikari, S., Ivins, E. R., Frederikse, T., Landerer, F. W., & Caron, L. (2019,
 708 May). Sea-level fingerprints emergent from GRACE mission data. *Earth*
 709 *System Science Data*, 11(2), 629–646. Retrieved 2022-07-21, from [https://](https://essd.copernicus.org/articles/11/629/2019/)
 710 essd.copernicus.org/articles/11/629/2019/ (Publisher: Copernicus
 711 GmbH) doi: 10.5194/essd-11-629-2019
- 712 Adhikari, S., Ivins, E. R., & Larour, E. (2016, March). ISSM-SESAW
 713 v1.0: mesh-based computation of gravitationally consistent sea-level and
 714 geodetic signatures caused by cryosphere and climate driven mass change.
 715 *Geoscientific Model Development*, 9(3), 1087–1109. Retrieved 2022-07-
 716 21, from <https://gmd.copernicus.org/articles/9/1087/2016/> doi:
 717 10.5194/gmd-9-1087-2016
- 718 Adler, R. F., Huffman, G. J., Chang, A. T. C., Ferraro, R., Xie, P., Janowiak,

- 719 J. E., ... Nelkin, E. (2003). The version 2 global precipitation climatology
 720 project (gpcp) monthly precipitation analysis (1979-present). *Journal of*
 721 *Hydrometeorology*. doi: 10.1175/1525-7541(2003)004<1147:tvgpcp>2.0.co;2
- 722 Argus, D. F., Peltier, W. R., Blewitt, G., & Kreemer, C. (2021). The
 723 Viscosity of the Top Third of the Lower Mantle Estimated Using
 724 GPS, GRACE, and Relative Sea Level Measurements of Glacial
 725 Isostatic Adjustment. *Journal of Geophysical Research: Solid Earth*,
 726 *126*(5), e2020JB021537. Retrieved 2023-01-13, from [https://](https://onlinelibrary.wiley.com/doi/abs/10.1029/2020JB021537)
 727 onlinelibrary.wiley.com/doi/abs/10.1029/2020JB021537 (eprint:
 728 <https://onlinelibrary.wiley.com/doi/pdf/10.1029/2020JB021537>) doi:
 729 10.1029/2020JB021537
- 730 Argus, D. F., Peltier, W. R., Drummond, R., & Moore, A. W. (2014, July). The
 731 Antarctica component of postglacial rebound model ICE-6G.c (VM5a) based
 732 on GPS positioning, exposure age dating of ice thicknesses, and relative
 733 sea level histories. *Geophysical Journal International*, *198*(1), 537–563.
 734 Retrieved 2023-01-12, from <https://doi.org/10.1093/gji/ggu140> doi:
 735 10.1093/gji/ggu140
- 736 Bettadpur, S. (2018). *Level-2 Gravity Field Product User Handbook* (User
 737 Handbook). Center for Space Research. Retrieved from [https://](https://podaac-tools.jpl.nasa.gov/drive/files/allData/grace/docs/L2-UserHandbook.v4.0.pdf)
 738 [podaac-tools.jpl.nasa.gov/drive/files/allData/grace/docs/](https://podaac-tools.jpl.nasa.gov/drive/files/allData/grace/docs/L2-UserHandbook.v4.0.pdf)
 739 [L2-UserHandbook.v4.0.pdf](https://podaac-tools.jpl.nasa.gov/drive/files/allData/grace/docs/L2-UserHandbook.v4.0.pdf)
- 740 Blazquez, A., Meyssignac, B., Lemoine, J.-M., Berthier, E., Ribes, A., & Cazenave,
 741 A. (2018). Exploring the uncertainty in GRACE estimates of the mass
 742 redistributions at the Earth surface: implications for the global water and
 743 sea level budgets. *Geophysical Journal International*. doi: 10.1093/gji/ggy293
- 744 Bonin, J. A., & Save, H. (2019). Evaluation of sub-monthly oceanographic signal in
 745 grace "daily" swath series using altimetry. *Ocean Science Discussions*. doi: 10
 746 .5194/os-16-423-2020
- 747 Bouih, M., Panet, I., Remy, D., Longuevergne, L., & Bonvalot, S. (2022). Deep
 748 mass redistribution prior to the 2010 mw 8.8 maule (chile) earthquake revealed
 749 by grace satellite gravity. *Earth and Planetary Science Letters*, *584*, 117465.
 750 Retrieved from [https://www.sciencedirect.com/science/article/pii/](https://www.sciencedirect.com/science/article/pii/S0012821X22001017)
 751 [S0012821X22001017](https://www.sciencedirect.com/science/article/pii/S0012821X22001017) doi: <https://doi.org/10.1016/j.epsl.2022.117465>

- 752 Caron, L., Ivins, E. R., Larour, E., Larour, E., Adhikari, S., Nilsson, J., ... Blewitt,
753 G. (2018). Gia model statistics for grace hydrology, cryosphere, and ocean
754 science. *Geophysical Research Letters*. doi: 10.1002/2017gl076644
- 755 Carrere, L., & Lyard, F. (2003). Modeling the barotropic response of the
756 global ocean to atmospheric wind and pressure forcing - comparisons with
757 observations. *Geophysical Research Letters*. doi: 10.1029/2002gl016473
- 758 Chen, J., Cazenave, A., Dahle, C., Llovel, W., Panet, I., Pfeffer, J., & Moreira,
759 L. (2022, February). Applications and Challenges of GRACE and GRACE
760 Follow-On Satellite Gravimetry. *Surveys in Geophysics*, 43(1), 305–345.
761 Retrieved 2022-07-21, from <https://doi.org/10.1007/s10712-021-09685-x>
762 doi: 10.1007/s10712-021-09685-x
- 763 Chen, J., Rodell, M., Wilson, C. R., & Famiglietti, J. S. (2005). Low degree
764 spherical harmonic influences on gravity recovery and climate experiment
765 (grace) water storage estimates. *Geophysical Research Letters*. doi:
766 10.1029/2005gl022964
- 767 Chen, J., Tapley, B., Tamisiea, M. E., Save, H., Wilson, C., Bettadpur, S.,
768 & Seo, K.-W. (2021). Error Assessment of GRACE and GRACE
769 Follow-On Mass Change. *Journal of Geophysical Research: Solid
770 Earth*, 126(9), e2021JB022124. Retrieved 2022-11-29, from [https://
771 onlinelibrary.wiley.com/doi/abs/10.1029/2021JB022124](https://onlinelibrary.wiley.com/doi/abs/10.1029/2021JB022124) (_eprint:
772 <https://onlinelibrary.wiley.com/doi/pdf/10.1029/2021JB022124>) doi:
773 10.1029/2021JB022124
- 774 Cheng, M., & Ries, J. C. (2017). The unexpected signal in grace estimates of c_{20} .
775 *Journal of Geodesy*. doi: 10.1007/s00190-016-0995-5
- 776 Cheng, M., Ries, J. C., & Tapley, B. D. (2011). Variations of the earth's figure axis
777 from satellite laser ranging and grace. *Journal of Geophysical Research*. doi: 10
778 .1029/2010jb000850
- 779 *CSR RL6.0*. (2018). Retrieved from [https://podaac.jpl.nasa.gov/dataset/
780 GRACE_GSM_L2_GRAV_CSR_RL06](https://podaac.jpl.nasa.gov/dataset/GRACE_GSM_L2_GRAV_CSR_RL06)
- 781 Dahle, C., Flechtner, F., Dobsław, H., Michalak, G., Neumayer, K.-H., Reinhold,
782 A., ... Sulzbach, R. (2019). The GFZ GRACE RL06 Monthly Gravity Field
783 Time Series: Processing Details and Quality Assessment. *Remote Sensing*. doi:
784 10.3390/rs11182116

- 785 Decharme, B., Delire, C., Minvielle, M., Colin, J., Vergnes, J., Alias, A., ...
 786 Voldoire, A. (2019). Recent changes in the isba-ctrip land surface system
 787 for use in the cnrm-cm6 climate model and in global off-line hydrological
 788 applications. *Journal of Advances in Modeling Earth Systems*. doi:
 789 10.1029/2018ms001545
- 790 Dee, D., Uppala, S., Simmons, A., Berrisford, P., Kobayashi, S., Andrae, U., ...
 791 Thépaut, J.-N. (2011). The era-interim reanalysis: configuration and
 792 performance of the data assimilation system. *Quarterly Journal of the Royal*
 793 *Meteorological Society*. doi: 10.1002/qj.828
- 794 Deggim, S., Eicker, A., Schawohl, L., Gerdener, H., Schulze, K., Engels, O.,
 795 ... Longuevergne, L. (2021, May). RECOG RL01: correcting GRACE
 796 total water storage estimates for global lakes/reservoirs and earthquakes.
 797 *Earth System Science Data*, 13(5), 2227–2244. Retrieved 2022-03-11, from <https://essd.copernicus.org/articles/13/2227/2021/> (Publisher:
 798 Copernicus GmbH) doi: 10.5194/essd-13-2227-2021
- 800 Dehant, V., Campuzano, S. A., De Santis, A., & van Westrenen, W. (2022,
 801 February). Structure, Materials and Processes in the Earth’s Core and Mantle.
 802 *Surveys in Geophysics*, 43(1), 263–302. Retrieved 2023-01-23, from [https://](https://doi.org/10.1007/s10712-021-09684-y)
 803 doi.org/10.1007/s10712-021-09684-y doi: 10.1007/s10712-021-09684-y
- 804 Dill, R. (2008). Hydrological model lsdm for operational earth rotation and gravity
 805 field variations. *null*. doi: 10.2312/gfz.b103-08095
- 806 Dill, R., Dill, R., Dobslaw, H., & Dobslaw, H. (2010). Short-term polar motion
 807 forecasts from earth system modeling data. *Journal of Geodesy*. doi: 10.1007/
 808 s00190-010-0391-5
- 809 Dill, R., & Dobslaw, H. (2013). Numerical simulations of global-scale high-
 810 resolution hydrological crustal deformations. *Journal of Geophysical*
 811 *Research: Solid Earth*, 118(9), 5008–5017. Retrieved 2022-06-23, from
 812 <https://onlinelibrary.wiley.com/doi/abs/10.1002/jgrb.50353>
 813 (_eprint: <https://onlinelibrary.wiley.com/doi/pdf/10.1002/jgrb.50353>) doi:
 814 10.1002/jgrb.50353
- 815 Dill, R., Klemann, V., & Dobslaw, H. (2018). Relocation of River Storage
 816 From Global Hydrological Models to Georeferenced River Channels for
 817 Improved Load-Induced Surface Displacements. *Journal of Geophysical*

- 818 *Research: Solid Earth*, 123(8), 7151–7164. Retrieved 2022-06-23, from
 819 <https://onlinelibrary.wiley.com/doi/abs/10.1029/2018JB016141>
 820 (_eprint: <https://onlinelibrary.wiley.com/doi/pdf/10.1029/2018JB016141>)
 821 doi: 10.1029/2018JB016141
- 822 Dobslaw, H., Bergmann-Wolf, I., Dill, R., Poropat, L., Thomas, M., Dahle, C.,
 823 ... Flechtner, F. (2017, October). A new high-resolution model of non-
 824 tidal atmosphere and ocean mass variability for de-aliasing of satellite gravity
 825 observations: AOD1B RL06. *Geophysical Journal International*, 211(1), 263–
 826 269. Retrieved 2022-07-21, from <https://doi.org/10.1093/gji/ggx302> doi:
 827 10.1093/gji/ggx302
- 828 Dobslaw, H., Bergmann-Wolf, I., Forootan, E., Dahle, C., Mayer-Gürr, T., Kusche,
 829 J., & Flechtner, F. (2015). Modeling of present-day atmosphere and ocean
 830 non-tidal de-aliasing errors for future gravity mission simulations. *Journal of*
 831 *Geodesy*. doi: 10.1007/s00190-015-0884-3
- 832 Dobslaw, H., Dill, R., Dill, R., Bagge, M., Klemann, V., Boergens, E., ... Flechtner,
 833 F. (2020). Gravitationally consistent mean barostatic sea level rise from
 834 leakage-corrected monthly grace data. *Journal of Geophysical Research*. doi:
 835 10.1029/2020jb020923
- 836 Dobslaw, H., Dobslaw, H., Flechtner, F., Bergmann-Wolf, I., Dahle, C., Dahle, C.,
 837 ... Thomas, M. (2013). Simulating high-frequency atmosphere-ocean mass
 838 variability for dealiasing of satellite gravity observations: Aod1b rl05. *Journal*
 839 *of Geophysical Research*. doi: 10.1002/jgrc.20271
- 840 Dumberry, M. (2010a). Gravity variations induced by core flows. *Geophysical*
 841 *Journal International*, 180(2), 635–650. Retrieved 2022-03-11, from
 842 <https://doi.org/10.1111/j.1365-246X.2009.04437.x> doi: 10.1111/
 843 j.1365-246X.2009.04437.x
- 844 Dumberry, M. (2010b, September). Gravitationally driven inner core differential
 845 rotation. *Earth and Planetary Science Letters*, 297(3-4), 387–394. Retrieved
 846 2022-10-25, from [https://linkinghub.elsevier.com/retrieve/pii/
 847 S0012821X10004152](https://linkinghub.elsevier.com/retrieve/pii/S0012821X10004152) doi: 10.1016/j.epsl.2010.06.040
- 848 Dumberry, M., & Bloxham, J. (2004a). Variations in the Earth's gravity field caused
 849 by torsional oscillations in the core. *Geophysical Journal International*, 159(2),
 850 417–434.

- 851 Dumberry, M., & Bloxham, J. (2004b, November). Variations in the Earth's
 852 gravity field caused by torsional oscillations in the core. *Geophysical*
 853 *Journal International*, 159(2), 417–434. Retrieved 2023-01-19, from
 854 <https://doi.org/10.1111/j.1365-246X.2004.02402.x> doi: 10.1111/
 855 [j.1365-246X.2004.02402.x](https://doi.org/10.1111/j.1365-246X.2004.02402.x)
- 856 Dumberry, M., & Manda, M. (2021). Gravity Variations and Ground Deformations
 857 Resulting from Core Dynamics. *Surveys in Geophysics*. Retrieved 2022-03-11,
 858 from <https://doi.org/10.1007/s10712-021-09656-2> doi: 10.1007/s10712
 859 -021-09656-2
- 860 Döll, P., Kaspar, F., & Lehner, B. (2003). A global hydrological model for
 861 deriving water availability indicators: model tuning and validation. *Journal*
 862 *of Hydrology*. doi: 10.1016/s0022-1694(02)00283-4
- 863 Frappart, F., Ramillien, G., Leblanc, M., Leblanc, M., Tweed, S., Bonnet, M.-P.,
 864 & Maisongrande, P. (2011). An independent component analysis filtering
 865 approach for estimating continental hydrology in the grace gravity data.
 866 *Remote Sensing of Environment*. doi: 10.1016/j.rse.2010.08.017
- 867 Gégout, P., Boy, J.-P., Hinderer, J., & Ferhat, G. (2010). Modeling and observation
 868 of loading contribution to time-variable GPS sites positions. In *Gravity, geoid*
 869 *and earth observation* (pp. 651–659). Springer.
- 870 Geruo, A., Wahr, J., & Zhong, S. (2013). Computations of the viscoelastic
 871 response of a 3-D compressible Earth to surface loading: an application to
 872 Glacial Isostatic Adjustment in Antarctica and Canada. *Geophysical Journal*
 873 *International*. doi: 10.1093/gji/ggs030
- 874 Gillet, N., Dumberry, M., & Rosat, S. (2020). The limited contribution from outer
 875 core dynamics to global deformations at the Earth's surface. *Geophysical*
 876 *Journal International*, 224, 216–229. doi: 10.1093/gji/ggaa448
- 877 Gillet, N., Gerick, F., Jault, D., Schwaiger, T., Aubert, J., & Iwas, M. (2022,
 878 March). Satellite magnetic data reveal interannual waves in Earth's core.
 879 *Proceedings of the National Academy of Sciences*, 119(13), e2115258119.
 880 Retrieved 2023-01-27, from [https://www.pnas.org/doi/abs/10.1073/
 881 \[pnas.2115258119\]\(https://www.pnas.org/doi/abs/10.1073/pnas.2115258119\)](https://www.pnas.org/doi/abs/10.1073/pnas.2115258119) (Publisher: Proceedings of the National Academy of
 882 Sciences) doi: 10.1073/pnas.2115258119

- 883 Gillet, N., Lesur, V., & Olsen, N. (2010, August). Geomagnetic Core Field Secular
 884 Variation Models. *Space Science Reviews*, 155(1), 129–145. Retrieved 2022-
 885 05-06, from <https://doi.org/10.1007/s11214-009-9586-6> doi: 10.1007/
 886 s11214-009-9586-6
- 887 Hersbach, H., Bell, B., Berrisford, P., Hirahara, S., Horanyi, A., Muñoz-Sabater, J.,
 888 ... Thépaut, J.-N. (2020). The era5 global reanalysis. *Quarterly Journal of*
 889 *the Royal Meteorological Society*. doi: 10.1002/qj.3803
- 890 Horwath, M., Gutknecht, B. D., Cazenave, A., Palanisamy, H. K., Marti, F.,
 891 Marzeion, B., ... Benveniste, J. (2022, February). Global sea-level budget and
 892 ocean-mass budget, with a focus on advanced data products and uncertainty
 893 characterisation. *Earth System Science Data*, 14(2), 411–447. Retrieved
 894 2022-07-21, from <https://essd.copernicus.org/articles/14/411/2022/>
 895 (Publisher: Copernicus GmbH) doi: 10.5194/essd-14-411-2022
- 896 Ilk, K.-H., Flury, J., Rummel, R., Schwintzer, P., Bosch, W., Haas, C., ... Gravity
 897 Field and Gravimetry 2009, G. C. (2004). *Mass Transport and Mass*
 898 *Distribution in the Earth System : Contribution of the New Generation*
 899 *of Satellite Gravity and Altimetry Missions to Geosciences; Proposal for a*
 900 *German Priority Research Program* (Tech. Rep.). Retrieved 2022-06-22, from
 901 [https://gfzpublic.gfz-potsdam.de/pubman/faces/ViewItemFullPage.jsp](https://gfzpublic.gfz-potsdam.de/pubman/faces/ViewItemFullPage.jsp?itemId=item_231104_1)
 902 [?itemId=item_231104_1](https://gfzpublic.gfz-potsdam.de/pubman/faces/ViewItemFullPage.jsp?itemId=item_231104_1) (Publisher: GOCE-Projektbüro Deutschland, Techn.
 903 Univ. München, GeoForschungsZentrum Potsdam)
- 904 Jault, D., & Finlay, C. C. (2015, January). 8.09 - Waves in the Core and
 905 Mechanical Core–Mantle Interactions. In G. Schubert (Ed.), *Treatise on*
 906 *Geophysics (Second Edition)* (pp. 225–244). Oxford: Elsevier. Retrieved
 907 2023-01-31, from [https://www.sciencedirect.com/science/article/pii/](https://www.sciencedirect.com/science/article/pii/B9780444538024001500)
 908 [B9780444538024001500](https://www.sciencedirect.com/science/article/pii/B9780444538024001500) doi: 10.1016/B978-0-444-53802-4.00150-0
- 909 Jekeli, C. (1981). Alternative methods to smooth the earth’s gravity field. *null*. doi:
 910 *null*
- 911 Jin, S., & Feng, G. (2013, July). Large-scale variations of global groundwater
 912 from satellite gravimetry and hydrological models, 2002–2012. *Global and*
 913 *Planetary Change*, 106, 20–30. Retrieved 2022-06-23, from [https://](https://linkinghub.elsevier.com/retrieve/pii/S0921818113000416)
 914 linkinghub.elsevier.com/retrieve/pii/S0921818113000416 doi:
 915 10.1016/j.gloplacha.2013.02.008

- 916 Jin, S., Hassan, A. A., & Feng, G. (2012). Assessment of terrestrial water
 917 contributions to polar motion from grace and hydrological models. *Journal*
 918 *of Geodynamics*. doi: 10.1016/j.jog.2012.01.009
- 919 *JPL RL6.0*. (2018). Retrieved from [https://podaac.jpl.nasa.gov/dataset/](https://podaac.jpl.nasa.gov/dataset/GRACE_GSM_L2_GRAV_JPL_RL06)
 920 [GRACE_GSM_L2_GRAV_JPL_RL06](https://podaac.jpl.nasa.gov/dataset/GRACE_GSM_L2_GRAV_JPL_RL06)
- 921 Jungclaus, J. H., Fischer, N., Haak, H., Lohmann, K., Marotzke, J., Matei, D., ...
 922 von Storch, J.-S. (2013). Characteristics of the ocean simulations in mpiom
 923 the ocean component of the mpi earth system model. *Journal of Advances in*
 924 *Modeling Earth Systems*. doi: 10.1002/jame.20023
- 925 Kappelsberger, M. T., Strößenreuther, U., Scheinert, M., Horwath, M., Groh,
 926 A., Knöfel, C., ... Khan, S. A. (2021). Modeled and observed bedrock
 927 displacements in north-east Greenland using refined estimates of present-day
 928 ice-mass changes and densified GNSS measurements. *Journal of Geophysical*
 929 *Research*. doi: 10.1029/2020jf005860
- 930 Koelemeijer, P. (2021). Toward consistent seismological models of the core–mantle
 931 boundary landscape. In *Mantle convection and surface expressions* (p. 229-
 932 255). American Geophysical Union (AGU). Retrieved from [https://](https://agupubs.onlinelibrary.wiley.com/doi/abs/10.1002/9781119528609.ch9)
 933 agupubs.onlinelibrary.wiley.com/doi/abs/10.1002/9781119528609.ch9
 934 doi: <https://doi.org/10.1002/9781119528609.ch9>
- 935 Kusche, J. (2007). Approximate decorrelation and non-isotropic smoothing of time-
 936 variable grace-type gravity field models. *Journal of Geodesy*. doi: 10.1007/
 937 [s00190-007-0143-3](https://doi.org/10.1007/s00190-007-0143-3)
- 938 Kusche, J., & Schrama, E. J. O. (2005). Surface mass redistribution
 939 inversion from global GPS deformation and Gravity Recovery and
 940 Climate Experiment (GRACE) gravity data. *Journal of Geophysical*
 941 *Research: Solid Earth*, 110(B9). Retrieved 2022-07-21, from [https://](https://onlinelibrary.wiley.com/doi/abs/10.1029/2004JB003556)
 942 onlinelibrary.wiley.com/doi/abs/10.1029/2004JB003556 (_eprint:
 943 <https://onlinelibrary.wiley.com/doi/pdf/10.1029/2004JB003556>) doi:
 944 10.1029/2004JB003556
- 945 Kvas, A., Behzadpour, S., Ellmer, M., Klinger, B., Strasser, S., Zehentner, N.,
 946 & Mayer-Gürr, T. (2019). Itsg-grace2018: Overview and evaluation
 947 of a new grace-only gravity field time series. *Journal of Geophysical*
 948 *Research: Solid Earth*, 124(8), 9332-9344. Retrieved from [https://](https://doi.org/10.1029/2018JB015000)

- 949 [agupubs.onlinelibrary.wiley.com/doi/abs/10.1029/2019JB017415](https://onlinelibrary.wiley.com/doi/abs/10.1029/2019JB017415) doi:
950 <https://doi.org/10.1029/2019JB017415>
- 951 Lambeck, K., Purcell, A. W., Zhao, J., Zhao, J., & Svensson, N.-O. (2010). The
952 scandinavian ice sheet: from mis 4 to the end of the last glacial maximum.
953 *Boreas*. doi: 10.1111/j.1502-3885.2010.00140.x
- 954 Lambeck, K., Rouby, H., Purcell, A. W., Sun, Y., & Sambridge, M. (2014). Sea
955 level and global ice volumes from the last glacial maximum to the holocene.
956 *Proceedings of the National Academy of Sciences of the United States of*
957 *America*. doi: 10.1073/pnas.1411762111
- 958 Landerer, F. W., Flechtner, F. M., Save, H., Webb, F. H., Bandikova, T., Bertiger,
959 W. I., ... Yuan, D.-N. (2020). Extending the Global Mass Change Data
960 Record: GRACE Follow-On Instrument and Science Data Performance.
961 *Geophysical Research Letters*, 47(12), e2020GL088306. Retrieved 2022-07-21,
962 from <https://onlinelibrary.wiley.com/doi/abs/10.1029/2020GL088306>
963 (_eprint: <https://onlinelibrary.wiley.com/doi/pdf/10.1029/2020GL088306>) doi:
964 10.1029/2020GL088306
- 965 Lemoine, J.-M., Biancale, R., Reinquin, F., Bourgogne, S., & Gégout, P. (2019).
966 *CNES/GRGS RL04 Earth gravity field models, from GRACE and SLR data*.
967 GFZ Data Services. Retrieved from [https://dataservices.gfz-potsdam.de/](https://dataservices.gfz-potsdam.de/icgem/showshort.php?id=escidoc:4656890)
968 [icgem/showshort.php?id=escidoc:4656890](https://dataservices.gfz-potsdam.de/icgem/showshort.php?id=escidoc:4656890) (Type: dataset) doi:
969 10.5880/ICGEM.2019.010
- 970 Lenczuk, A., Leszczuk, G., Klos, A., Kosek, W., & Bogusz, J. (2020, October).
971 Study on the inter-annual hydrology-induced deformations in Europe using
972 GRACE and hydrological models. *Journal of Applied Geodesy*, 14(4),
973 393–403. Retrieved 2022-06-23, from [https://www.degruyter.com/](https://www.degruyter.com/document/doi/10.1515/jag-2020-0017/html)
974 [document/doi/10.1515/jag-2020-0017/html](https://www.degruyter.com/document/doi/10.1515/jag-2020-0017/html) (Publisher: De Gruyter)
975 doi: 10.1515/jag-2020-0017
- 976 Liu, R., She, D., Li, M., & Wang, T. (2019). Using satellite observations to
977 assess applicability of gldas and wghm hydrological model. *Geomatics and*
978 *Information Science of Wuhan University*, 44(1671?8860(2019)11?1596?09),
979 1596. Retrieved from [http://ch.whu.edu.cn/en/article/doi/10.13203/](http://ch.whu.edu.cn/en/article/doi/10.13203/j.whugis20190108)
980 [j.whugis20190108](http://ch.whu.edu.cn/en/article/doi/10.13203/j.whugis20190108) doi: 10.13203/j.whugis20190108

- 981 Loomis, B. D., Luthcke, S. B., & Sabaka, T. J. (2019b, September). Regularization
 982 and error characterization of GRACE mascons. *Journal of Geodesy*, *93*(9),
 983 1381–1398. Retrieved 2022-12-01, from [https://doi.org/10.1007/](https://doi.org/10.1007/s00190-019-01252-y)
 984 [s00190-019-01252-y](https://doi.org/10.1007/s00190-019-01252-y) doi: 10.1007/s00190-019-01252-y
- 985 Loomis, B. D., Rachlin, K. E., & Luthcke, S. B. (2019a). Improved earth
 986 oblateness rate reveals increased ice sheet losses and mass-driven sea level
 987 rise. *Geophysical Research Letters*. doi: 10.1029/2019gl082929
- 988 Loomis, B. D., Wiese, D. N., Landerer, F. W., Rachlin, K. E., & Luthcke, S. B.
 989 (2020). Replacing grace/grace-fo with satellite laser ranging: Impacts
 990 on antarctic ice sheet mass change. *Geophysical Research Letters*. doi:
 991 10.1029/2019gl085488
- 992 Mandea, M., Narteau, C., Panet, I., & Le Mouél, J.-L. (2015). Gravimetric
 993 and magnetic anomalies produced by dissolution-crystallization at
 994 the core-mantle boundary. *Journal of Geophysical Research: Solid*
 995 *Earth*, *120*(9), 5983–6000. Retrieved 2022-03-11, from [https://](https://onlinelibrary.wiley.com/doi/abs/10.1002/2015JB012048)
 996 onlinelibrary.wiley.com/doi/abs/10.1002/2015JB012048 (eprint:
 997 <https://onlinelibrary.wiley.com/doi/pdf/10.1002/2015JB012048>) doi:
 998 10.1002/2015JB012048
- 999 Mandea, M., Panet, I., Lesur, V., de Viron, O., Diament, M., & Le Mouél, J.-
 1000 L. (2012, November). Recent changes of the Earth’s core derived from
 1001 satellite observations of magnetic and gravity fields. *Proceedings of the*
 1002 *National Academy of Sciences*, *109*(47), 19129–19133. Retrieved 2022-03-
 1003 11, from <https://www.pnas.org/doi/full/10.1073/pnas.1207346109>
 1004 (Publisher: Proceedings of the National Academy of Sciences) doi:
 1005 10.1073/pnas.1207346109
- 1006 Marti, F., Blazquez, A., Meyssignac, B., Ablain, M., Barnoud, A., Fraudeau, R., ...
 1007 Benveniste, J. (2022, January). Monitoring the ocean heat content change
 1008 and the Earth energy imbalance from space altimetry and space gravimetry.
 1009 *Earth System Science Data*, *14*(1), 229–249. Retrieved 2022-07-21, from
 1010 <https://essd.copernicus.org/articles/14/229/2022/> (Publisher:
 1011 Copernicus GmbH) doi: 10.5194/essd-14-229-2022
- 1012 Mayer-Gürr, T., Behzadpour, S., Ellmer, M., Klinger, B., Zehentner, N., Kvas, A.,
 1013 & Strasser, S. (2018). Itsg-grace2018: Monthly, daily and static gravity field

- 1014 solutions from grace. *null*. doi: 10.5880/icgem.2018.003
- 1015 Melini, D., & Spada, G. (2019). Some remarks on Glacial Isostatic Adjustment
1016 modelling uncertainties. *Geophysical Journal International*. doi: 10.1093/gji/
1017 ggz158
- 1018 Meyer, U., Lasser, M., Jaeggi, A., Dahle, C., Dahle, C., Flechtner, F., ...
1019 Bourgogne, S. (2020). International combination service for time-
1020 variable gravity fields (cost-g) monthly grace-fo series. *null*. doi: 10.5880/
1021 icgem.cost-g.002
- 1022 Panet, I., Bonvalot, S., Narteau, C., Remy, D., & Lemoine, J.-M. (2018, May).
1023 Migrating pattern of deformation prior to the Tohoku-Oki earthquake revealed
1024 by GRACE data. *Nature Geoscience*, *11*(5), 367–373. Retrieved 2022-03-11,
1025 from <https://www.nature.com/articles/s41561-018-0099-3> (Number: 5
1026 Publisher: Nature Publishing Group) doi: 10.1038/s41561-018-0099-3
- 1027 Peltier, W. R. (2004). Global glacial isostasy and the surface of the ice-age earth:
1028 The ice-5g (vm2) model and grace. *Annual Review of Earth and Planetary
1029 Sciences*. doi: 10.1146/annurev.earth.32.082503.144359
- 1030 Peltier, W. R., Argus, D. F., & Drummond, R. (2015). Space geodesy constrains
1031 ice age terminal deglaciation: The global ICE-6G.C (VM5a) model. *Journal of
1032 Geophysical Research*. doi: 10.1002/2014jb011176
- 1033 Peltier, W. R., Argus, D. F., & Drummond, R. (2018). Comment on “An
1034 Assessment of the ICE-6G.C (VM5a) Glacial Isostatic Adjustment Model”
1035 by Purcell et al. *Journal of Geophysical Research*. doi: 10.1002/2016jb013844
- 1036 Petrov, L., & Boy, J.-P. (2004). Study of the atmospheric pressure loading signal in
1037 VLBI observations. *Journal of Geophysical Research*, *109*(B03405).
- 1038 Pfeffer, J., Cazenave, A., & Barnoud, A. (2021). Analysis of the interannual
1039 variability in satellite gravity solutions: detection of climate modes in water
1040 mass displacements across continents and oceans. *Climate Dynamics*. doi:
1041 10.1007/s00382-021-05953-z
- 1042 Pfeffer, J., Cazenave, A., Blazquez, A., Decharme, B., Munier, S., & Barnoud, A.
1043 (2022, December). Detection of slow changes in terrestrial water storage
1044 with GRACE and GRACE-FO satellite gravity missions. *EGUsphere*, 1–
1045 85. Retrieved 2023-01-27, from [https://egusphere.copernicus.org/
1046 preprints/2022/egusphere-2022-1032/](https://egusphere.copernicus.org/preprints/2022/egusphere-2022-1032/) (Publisher: Copernicus GmbH)

- 1047 doi: 10.5194/egusphere-2022-1032
- 1048 Purcell, A., Dehecq, A., Tregoning, P., Potter, E.-K., McClusky, S. C.,
 1049 & Lambeck, K. (2011). Relationship between glacial isostatic
 1050 adjustment and gravity perturbations observed by GRACE. *Geophysical*
 1051 *Research Letters*, 38(18). Retrieved 2022-03-11, from [https://](https://onlinelibrary.wiley.com/doi/abs/10.1029/2011GL048624)
 1052 onlinelibrary.wiley.com/doi/abs/10.1029/2011GL048624 (eprint:
 1053 <https://onlinelibrary.wiley.com/doi/pdf/10.1029/2011GL048624>) doi:
 1054 10.1029/2011GL048624
- 1055 Richter, H. M. P., Lück, C., Klos, A., Sideris, M. G., Rangelova, E., & Kusche, J.
 1056 (2021). Reconstructing GRACE-type time-variable gravity from the Swarm
 1057 satellites. *Scientific Reports*, 11. Retrieved from [https://doi.org/10.1038/](https://doi.org/10.1038/s41598-020-80752-w)
 1058 [s41598-020-80752-w](https://doi.org/10.1038/s41598-020-80752-w) doi: 10.1038/s41598-020-80752-w
- 1059 Rodell, M., Famiglietti, J. S., Wiese, D. N., Reager, J. T., Beaulieu, H. K.,
 1060 Landerer, F. W., & Lo, M.-H. (2018, May). Emerging trends in global
 1061 freshwater availability. *Nature*, 557(7707), 651–659. Retrieved 2022-07-21,
 1062 from <https://www.nature.com/articles/s41586-018-0123-1> (Number:
 1063 7707 Publisher: Nature Publishing Group) doi: 10.1038/s41586-018-0123-1
- 1064 Rodell, M., Houser, P., Jambor, U., Gottschalck, J., Mitchell, K., Meng, C.-J., ...
 1065 others (2004). The global land data assimilation system. *Bulletin of the*
 1066 *American Meteorological Society*, 85(3), 381–394.
- 1067 Rosat, S., Gillet, N., Boy, J.-P., Couhert, A., & Dumberry, M. (2021, February).
 1068 Interannual variations of degree 2 from geodetic observations and surface
 1069 processes. *Geophysical Journal International*, 225(1), 200–221. Retrieved
 1070 2022-03-11, from <https://doi.org/10.1093/gji/ggaa590> doi: 10.1093/gji/
 1071 [ggaa590](https://doi.org/10.1093/gji/ggaa590)
- 1072 Saraswati, A. T., de Viron, O., & Manda, M. (2022, June). *Estimation des signaux*
 1073 *communs de la gravité spatiale et du champ magnétique liés à la variation*
 1074 *du champ du noyau terrestre* [Poster]. Congrès national de gravimétrie
 1075 spatiale du champ variable, Marseille. Retrieved 2022-07-27, from [https://](https://gravimetriefr.sciencesconf.org/browse/session?sessionid=71661)
 1076 gravimetriefr.sciencesconf.org/browse/session?sessionid=71661
- 1077 Scanlon, B. R., Zhang, Z., Save, H., Sun, A. Y., Schmied, H. M., Beek, L. P. H. v.,
 1078 ... Bierkens, M. F. P. (2018, February). Global models underestimate large
 1079 decadal declining and rising water storage trends relative to GRACE satellite

- 1080 data. *Proceedings of the National Academy of Sciences*, 115(6), E1080–E1089.
 1081 Retrieved 2021-07-29, from <https://www.pnas.org/content/115/6/E1080>
 1082 (Publisher: National Academy of Sciences Section: PNAS Plus) doi:
 1083 10.1073/pnas.1704665115
- 1084 Scanlon, B. R., Zhang, Z., Save, H., Wiese, D. N., Landerer, F. W., Long, D.,
 1085 ... Chen, J. (2016). Global evaluation of new grace mascon products for
 1086 hydrologic applications. *Water Resources Research*, 52(12), 9412–9429.
 1087 Retrieved from [https://agupubs.onlinelibrary.wiley.com/doi/abs/](https://agupubs.onlinelibrary.wiley.com/doi/abs/10.1002/2016WR019494)
 1088 10.1002/2016WR019494 doi: <https://doi.org/10.1002/2016WR019494>
- 1089 Schindelegger, M., Harker, A., Ponte, R. M., Dobsław, H., & Salstein, D. A.
 1090 (2021). Convergence of daily grace solutions and models of submonthly
 1091 ocean bottom pressure variability. *Journal of Geophysical Research*. doi:
 1092 10.1029/2020jc017031
- 1093 Schmeer, M., Schmidt, M., Bosch, W., & Seitz, F. (2012). Separation of mass signals
 1094 within grace monthly gravity field models by means of empirical orthogonal
 1095 functions. *Journal of Geodynamics*. doi: 10.1016/j.jog.2012.03.001
- 1096 Schmied, H. M., Cáceres, D., Eisner, S., Flörke, M., Niemann, C., Peiris, T. A., ...
 1097 Döll, P. (2020, March). *The global freshwater availability and water use model*
 1098 *WaterGAP 2.2d* (Tech. Rep. No. EGU2020-11434). Copernicus Meetings.
 1099 Retrieved 2022-07-27, from [https://meetingorganizer.copernicus.org/](https://meetingorganizer.copernicus.org/EGU2020/EGU2020-11434.html)
 1100 EGU2020/EGU2020-11434.html (Conference Name: EGU2020) doi:
 1101 10.5194/egusphere-egu2020-11434
- 1102 Schneider, U., Becker, A., Finger, P., Meyer-Christoffer, A., Rudolf, B., & Ziese,
 1103 M. (2016). Gpcc full data reanalysis version 7.0: Monthly land-surface
 1104 precipitation from rain gauges built on gts based and historic data. *null*.
 1105 doi: 10.5065/d6000072
- 1106 Sośnica, K., Jäggi, A., Meyer, U., Thaller, D., Beutler, G., Arnold, D., & Dach,
 1107 R. (2015, October). Time variable Earth's gravity field from SLR satellites.
 1108 *Journal of Geodesy*, 89(10), 945–960. Retrieved 2021-01-25, from [https://](https://doi.org/10.1007/s00190-015-0825-1)
 1109 doi.org/10.1007/s00190-015-0825-1 doi: 10.1007/s00190-015-0825-1
- 1110 Swenson, S., & Wahr, J. (2002). Methods for inferring regional surface-mass
 1111 anomalies from gravity recovery and climate experiment (grace) measurements
 1112 of time-variable gravity. *Journal of Geophysical Research*. doi: 10.1029/

- 1113 2001jb000576
- 1114 Tapley, B. D., Bettadpur, S., Ries, J. C., Thompson, P. F., & Watkins, M. M. (2004,
1115 July). GRACE Measurements of Mass Variability in the Earth System.
1116 *Science*, *305*(5683), 503–505. Retrieved 2022-07-21, from [https://www](https://www.science.org/doi/full/10.1126/science.1099192)
1117 [.science.org/doi/full/10.1126/science.1099192](https://www.science.org/doi/full/10.1126/science.1099192) (Publisher: American
1118 Association for the Advancement of Science) doi: 10.1126/science.1099192
- 1119 Tapley, B. D., Watkins, M. M., Flechtner, F., Reigber, C., Bettadpur, S., Rodell,
1120 M., ... Velicogna, I. (2019, May). Contributions of GRACE to understanding
1121 climate change. *Nature Climate Change*, *9*(5), 358–369. Retrieved 2022-05-03,
1122 from <https://www.nature.com/articles/s41558-019-0456-2> (Number: 5
1123 Publisher: Nature Publishing Group) doi: 10.1038/s41558-019-0456-2
- 1124 Velicogna, I., Mohajerani, Y., A, G., Mouginot, J., Noël, B., Sutterley, T. C., ...
1125 van Wessem, J. M. (2020). Continuity of ice sheet mass loss in greenland and
1126 antarctica from the grace and grace follow-on missions. *Geophysical Research*
1127 *Letters*. doi: 10.1029/2020gl087291
- 1128 Wahr, J., Molenaar, M., & Bryan, F. (1998). Time variability of the Earth's gravity
1129 field: Hydrological and oceanic effects and their possible detection using
1130 GRACE. *Journal of Geophysical Research: Solid Earth*, *103*(B12), 30205–
1131 30229. Retrieved 2020-11-06, from [https://agupubs.onlinelibrary.wiley](https://agupubs.onlinelibrary.wiley.com/doi/abs/10.1029/98JB02844)
1132 [.com/doi/abs/10.1029/98JB02844](https://agupubs.onlinelibrary.wiley.com/doi/abs/10.1029/98JB02844) (Formules EWH, conversion bizarre Cnm,
1133 Snm en N hauteur geoide) doi: 10.1029/98JB02844
- 1134 Wang, F., Shen, Y., Chen, Q., & Sun, Y. (2021). Reduced misclosure of global sea-
1135 level budget with updated tongji-grace2018 solution. *Scientific Reports*. doi: 10
1136 [.1038/s41598-021-96880-w](https://doi.org/10.1038/s41598-021-96880-w)
- 1137 Whitehouse, P. L., Bentley, M. J., Milne, G. A., King, M. A., & Thomas, I. D.
1138 (2012). A new glacial isostatic adjustment model for antarctica: calibrated
1139 and tested using observations of relative sea-level change and present-day uplift
1140 rates. *Geophysical Journal International*. doi: 10.1111/j.1365-246x.2012.05557
1141 [.x](https://doi.org/10.1111/j.1365-246x.2012.05557.x)
- 1142 Śliwińska, J., Nastula, J., & Wińska, M. (2021). Evaluation of hydrological and
1143 cryospheric angular momentum estimates based on GRACE, GRACE-FO and
1144 SLR data for their contributions to polar motion excitation. *Earth, Planets*
1145 *and Space*. doi: 10.1186/s40623-021-01393-5

Figure 1.

Time scales

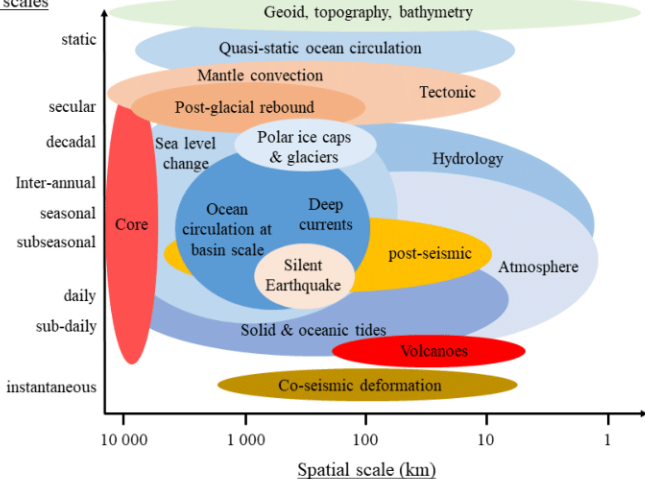
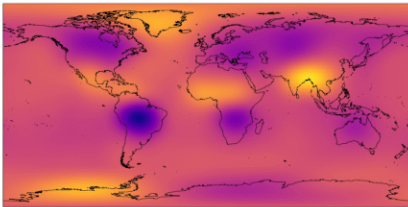
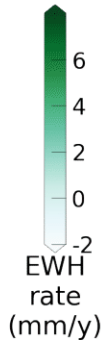
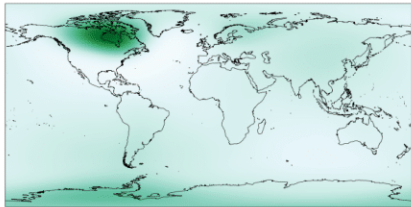
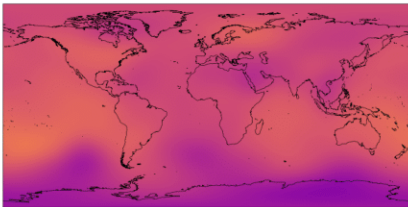
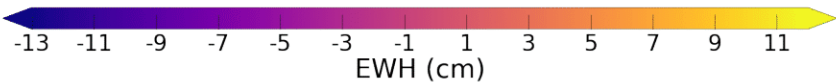
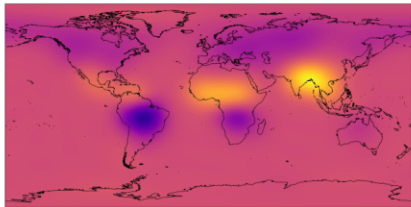


Figure 2.

GRACE (COST-G)**GIA (ICE-6G_D)**

EWH
rate
(mm/y)

AOD1B**ISBA**

EWH (cm)

Figure 3.

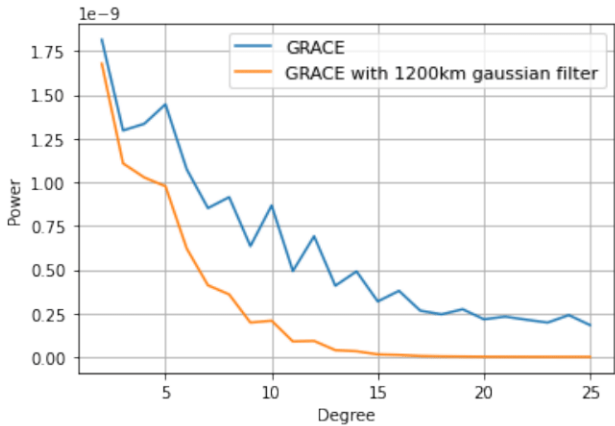
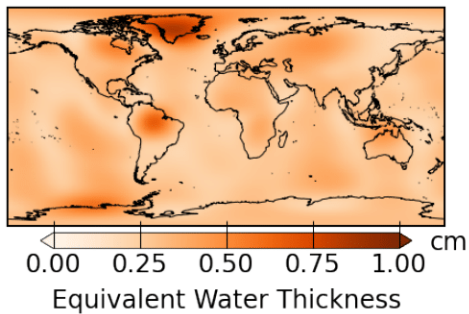
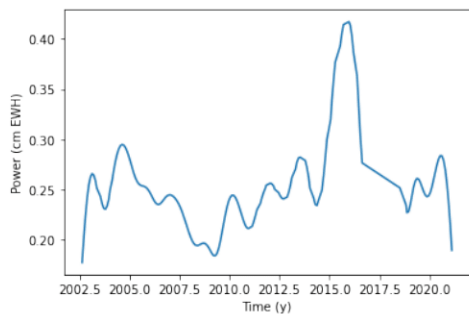


Figure 4.



(a) Average of RMS differences in cm EWH spatially represented



(b) Average of RMS differences in cm EWH represented trough time

Figure 5.

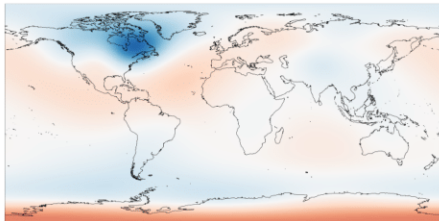
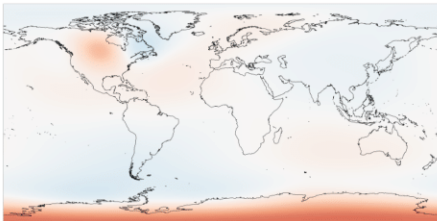
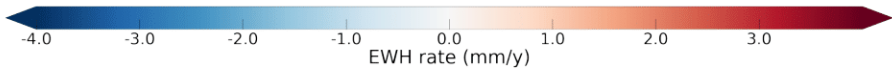
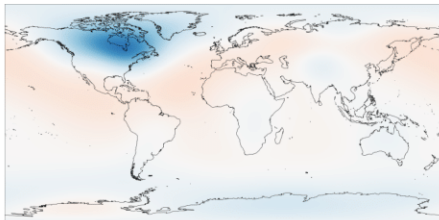
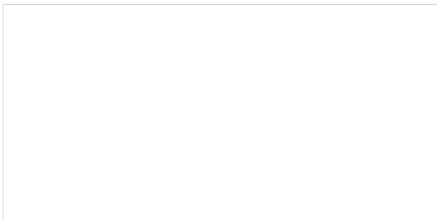
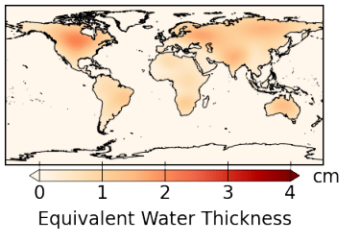
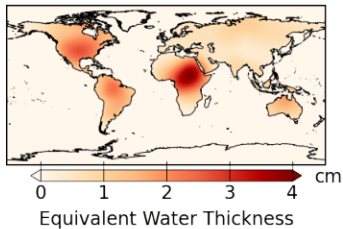
ICE-6G_D**Caron18****A13****ICE-6G_D**

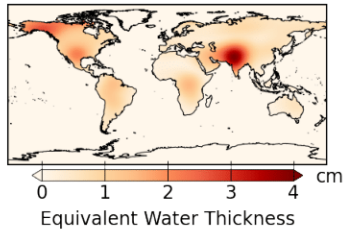
Figure 6.



(a) ERA5 minus
GLDAS

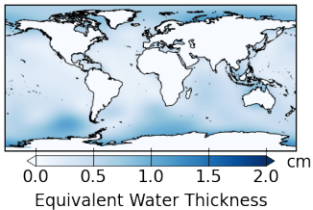


(b) ISBA minus
LSDM

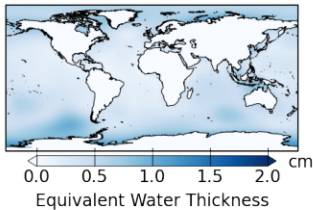


(c) ISBA minus
WGHM

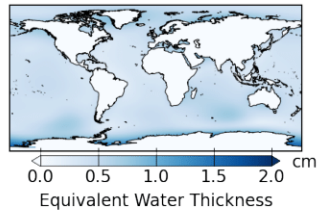
Figure 7.



(a) OMCT

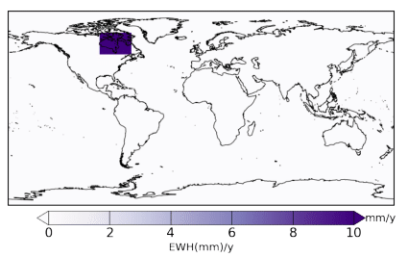


(b) MPIOM

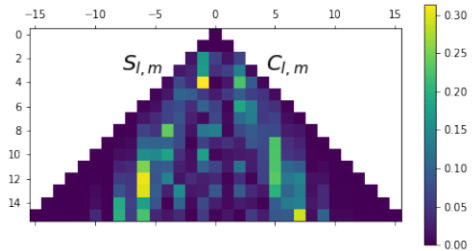


(c) T-UGOm

Figure 8.

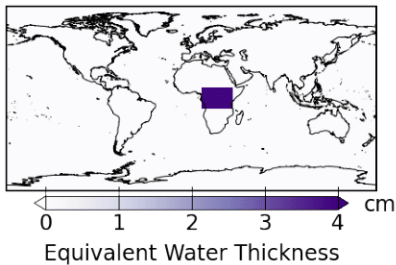


(a) Synthetic signal in North America in EWH

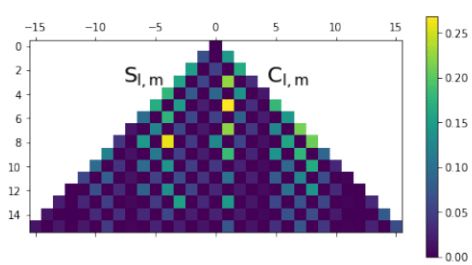


(b) SH power normalized by GRACE standard deviation up to degree 15

Figure 9.

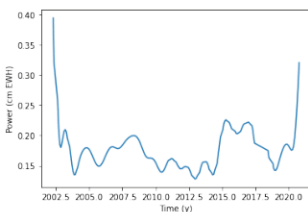


(a) Synthetic 3-yr signal over Africa with an amplitude of 4 cm EWH

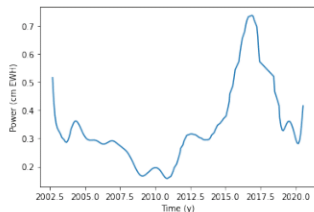


(b) SH power normalized by GRACE standard deviation up to degree 15

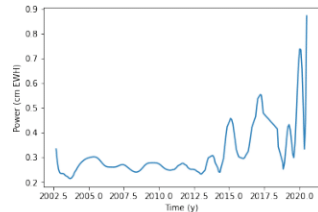
Figure A1.



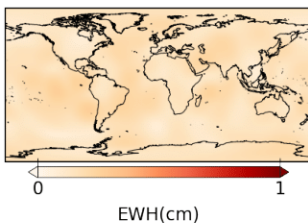
(a) Temporal RMS difference between CSR and JPL solutions



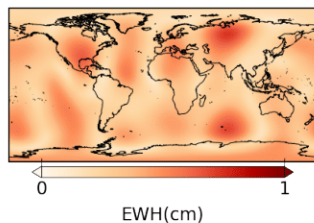
(b) Temporal RMS difference between CSR and GFZ solutions



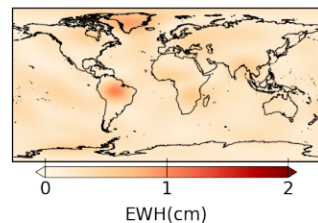
(c) Temporal RMS difference between CSR and GRAZ solutions



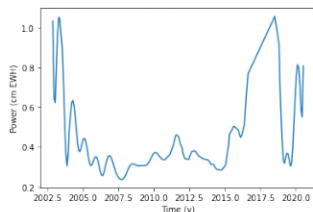
(d) Spatial RMS difference between CSR and JPL solutions



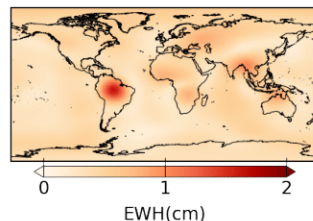
(e) Spatial RMS difference between CSR and GFZ solutions



(f) Spatial RMS difference between CSR and GRAZ solutions



(g) Temporal RMS difference between CSR and CNES solutions



(h) Spatial RMS difference between CSR and CNES solutions

Figure B1.

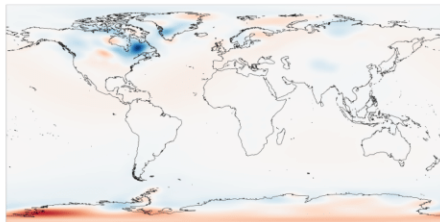
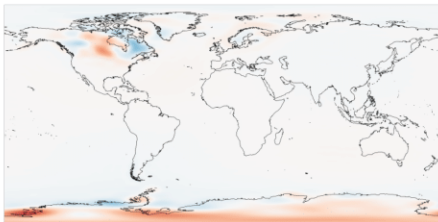
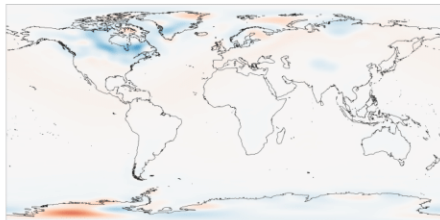
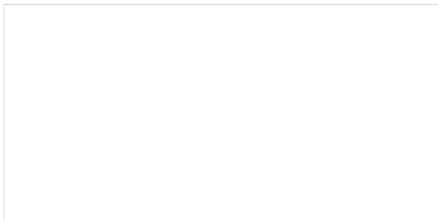
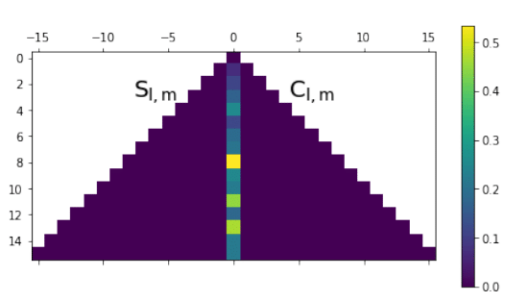
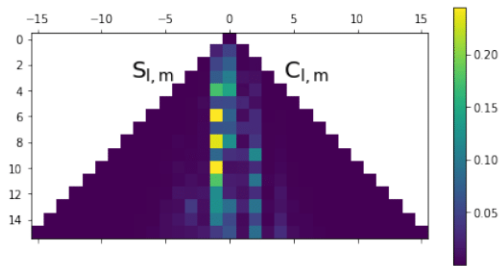
ICE-6G_D**Caron18****A13****ICE-6G_D**

Figure E1.

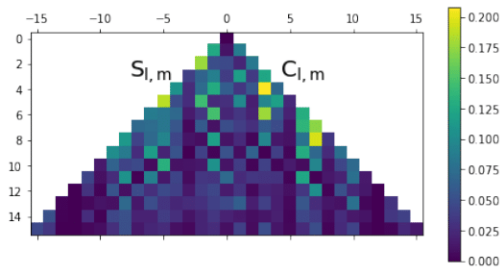


(a) Case n^o2 with synthetic signal under -80° of latitude

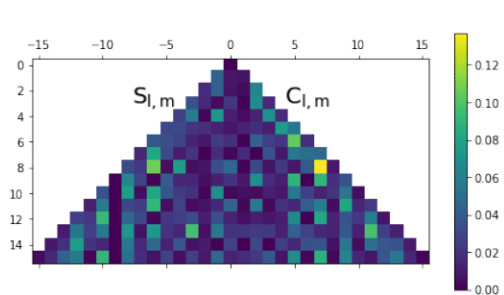


(b) Case n^o3 with synthetic signal under -70° of latitude and between -160° and -30° of longitude

Figure F1.



(a) Case $n^o 2$ with synthetic signal over Amazon forest



(b) Case $n^o 3$ with synthetic signal over India